ACS APPLIED NANO MATERIALS

www.acsanm.org Article

Silver/Iron Oxide Nano-Popcorns for Imaging and Therapy

Ateeque ur Rehman, Yuao Wu,[#] Huong D. N. Tran,[#] Karla Vazquez-Prada, Yajun Liu, Hossein Adelnia, Nyoman D. Kurniawan, Muhammad Naeem Anjum, Shehzahdi S. Moonshi, and Hang T. Ta*

Cite This: https://doi.org/10.1021/acsanm.1c01571 Read Online

ACCESS | Metrics & More | Article Recommendations | Supporting Information

ABSTRACT: We have for the first time reported 120 nm silver/iron oxide hybrid nano-popcorns with surface plasmon resonance tuned at near-infrared (NIR) range for imaging and therapeutic applications. The nano-popcorns displayed excellent photothermal thrombolytic effect and anticancer activity in a concentration-dependent manner upon NIR laser irradiation, benefiting the photothermal treatment of thrombosis and cancer. At low concentrations, the nano-popcorns exhibited relatively good reactive oxygen species (ROS) scavenging capability. Notably, the nano-popcorns exerted excellent magnetic resonance imaging (MRI) T_2-signal after being sequestered within cells or binding on the surface of the thrombus, becoming a promising imaging agent for cell labeling and thrombus detection. Cytotoxicity, biodistribution studies, and histology analysis demonstrated no significant toxicity caused by the nano-popcorns. There was no long-term retention of the nano-popcorns in the mouse organs at the dose treated. These results give insight into the potential of using these nano-popcorns for diagnosis and treatment of diseases related to ROS, cancer, and thrombosis.

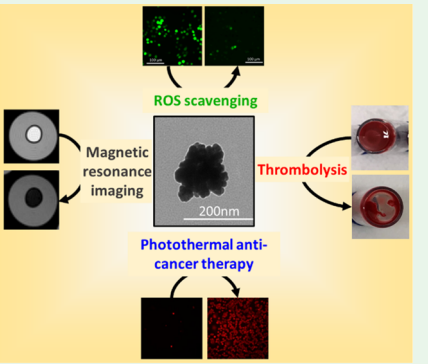

KEYWORDS: *silver-coated iron oxide, theranostics, cancer, reactive oxygen species, thrombosis*

1. INTRODUCTION

Nanomedicine encompasses the use of submicrometer-sized tools for detecting, treating, and preventing diseases.[1] Much effort has been made in nanotechnology for therapeutic purposes with the aims of improving targeting and efficacy while minimizing side effects of disease treatment. In the past years, strategies for visualizing and quantifying pathological processes have also been explored.[2] More importantly, recent attempts have been made to develop nanomaterials with simultaneous noninvasive diagnostic and therapeutic activities. These nanotheranostics are designed to improve and accelerate new strategies to speed up preclinical development, achieve better treatment outcomes, and monitor treatment of diseases.[3−5]

Magnetic resonance imaging (MRI) is one of the preferred modalities for disease diagnosis and treatment monitoring.[6−9] Unlike other imaging techniques, MRI provides deep tissue penetration, high spatial resolution, and does not rely on the use of hazardous radiation.[10−12] The principal motivation for molecular MRI is the improvement of specificity with the utilization of contrast agents.[13,14] Iron oxide nanoparticles (IONPs) are the most commonly used nanomaterials that can enhance molecular MRI by shortening MRI T_2-signal.[15−30]

Silver nanoparticles (AgNPs) have been proven to possess promising characteristics suitable for biomedical applications, including antifungal, antibacterial, antiviral, anti-inflammatory, antithrombosis, antiangiogenic, anticancer, and ability to accelerate wound healing.[31,32] Recently, the ability of AgNPs to downregulate the cellular ROS level has been reported.[33,34] Silver is also a promising nanomaterial for photothermal therapy owing to its unique surface plasmon resonance (SPR) property whereby surface oscillation of conduction electrons upon the excitation of incident light causes energy absorption enhancement and temperature increment.[35,36] Typically, silver-based nanoparticles can be administrated to the target sites and enable photothermal light-to-heat conversion, leading to elevated local temperature that can kill abnormal cells/tissues while minimizing damage to normal cells and surrounding tissues.[37,38] Hence, photothermal therapy mediated by nanoparticles having SPR effect potentially provides a minimally invasive treatment strategy accompanied with high specificity and reduced adverse effects.[37−39] Thus, this therapeutic approach has been considered as a great treatment strategy for diseases like atherosclerosis and cancer.[40−45] Moreover, nanoparticles having SPR effects are starting to gain attention as they have demonstrated good thrombolytic effect, which is highly advantageous for thrombosis treatment.[46] Nevertheless, the majority of research has focused on the utilization of gold-based nanoparticles and carbon nanotubes in spite of silver displaying the highest efficiency of SPR in the visible

Received: June 15, 2021
Accepted: August 19, 2021

Scheme 1. Development of Novel Multifunctional Silver/Iron Oxide Hybrid Nano-popcorns with Excellent Magnetic Resonance Contrast Effect, Good ROS Scavenging Capability, Promising Photothermal Thrombolysis Property, and Strong Photothermal Anticancer Activity

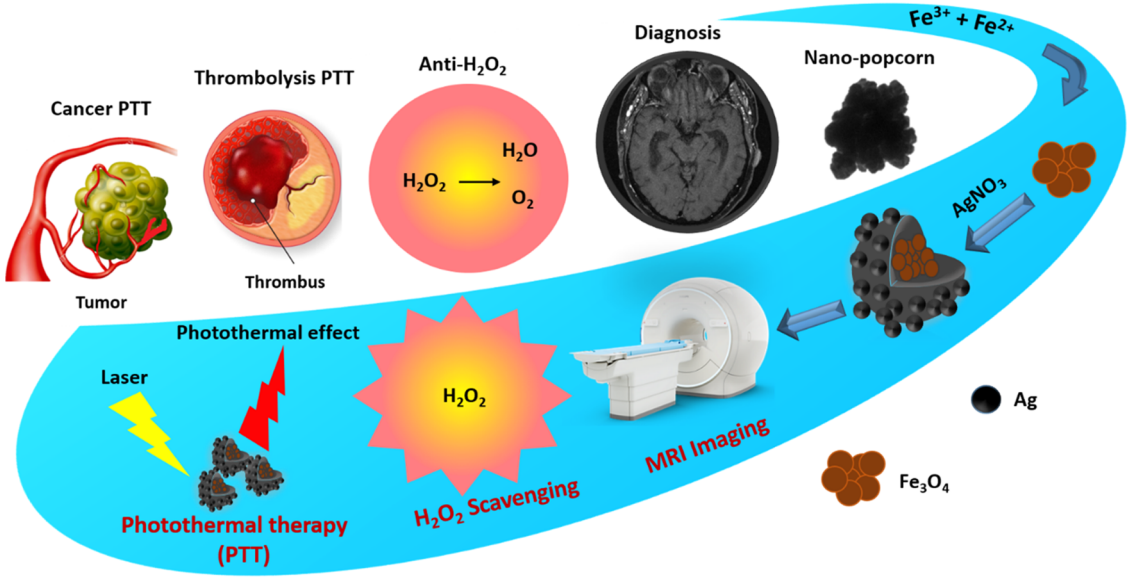

range.[40−45,47] In comparison to visible light, NIR laser poses lesser invasive damage to tissues and maximizes deep tissue penetration due to the slight absorption and scattering capacity in the NIR window of tissue components, which makes it optimal for biomedical applications.[48] To date, there is no hybrid NP based on Ag and Fe having SPR that can be tuned to the NIR range to the best of our knowledge.

Multifunctional theranostic nanoparticles have shown greater potential than the conventional as they can provide both disease diagnosis and treatment simultaneously and synergistically.[49] Theranostics strategy also allows tracking of the therapy and monitoring the distribution of the therapeutic agents. In this study, a novel theranostic silver/iron oxide hybrid nano-popcorn stabilized by polyacrylic acid (Ag@IO-PAA) was synthesized, in which the IO component functions as a good MRI contrast agent in imaging of cancer cells, macrophages, and thrombus, while Ag provides therapeutic potential in the treatment of diseases associated with ROS, cancer, and thrombosis (Scheme 1). Importantly, SPR of Ag@IO-PAA nano-popcorn was successfully tuned to display a strong absorbance in the NIR region, resulting in remarkable thrombolytic activity and anticancer effect via photothermal ablation of an 808 nm infrared laser. Additionally, the nano-popcorns exhibited efficient ROS scavenging capability when tested with buffer solution and J774A.1 macrophage. Also, nano-popcorns showed no significant signs of toxicity when tested *in vitro* and *in vivo* at the doses used in the study.

2. METHODS

The detailed experimental methods are described in the SI.

2.1. Synthesis and Characterization of Silver/Iron Oxide Hybrid Nano-Popcorn (Ag@IO). IONPs were synthesized using a high-temperature co-precipitation method. To obtain the silver coating on the surface of the IONPs, a $AgNO_3$ solution was prepared followed by the addition of the IONPs synthesized before. The elemental silver was seeded and reduced on the surface of IONPs by hydroxylamine (HDX), and TSC was added to stabilize the nanoparticles. The dense silver/iron oxide NPs (Ag@IOs) were separated from the less dense uncoated particles by centrifugation and then dialyzed against water overnight to remove any unreacted reagents. Ag@IOs were then coated with thiolated PAA. For platelet targeting, the resultant Ag@IO-PAA was conjugated with RGD peptide using carbodiimide chemistry, resulting in Ag@IO-PAA-RGD.

2.2. Cell-Based Assays (Cytotoxicity Study and ROS Scavenging). Chinese hamster ovary (CHO) and MDA-MB-231 cells were employed for cytotoxicity study. PrestoBlue and ethidium homodimer-1 were used to evaluate cell viability and proliferation. Macrophage J774A.1 was employed for ROS scavenging investigation. Cellular ROS was evaluated with 2′,7′-dichlorofluorescein diacetate (DCFDA) as previously described.[50]

2.3. *In Vitro* Cell and Thrombus MRI. Cancer cells (MDA-MB-231) and macrophages (J774A.1) were seeded in six-well plates at densities of 2×10^5 and 3×10^5 cells/well, respectively. After 24 h, the cells were treated with Ag@IO-PAA (0.1 mg/mL) for 12 h. The cells were then collected, washed, and embedded in agarose gel for MRI.

In vitro thrombus was prepared with fresh frozen plasma (obtained from Australian Red Cross Blood Service). Ag@IO-PAA-RGD nanoparticle dispersion was added on top of the thrombus, and the tube was incubated with gentle rotation for 1 h at 37 °C. The thrombus was then washed three times with PBS and embedded under agarose gel for MRI.

2.4. Photothermal Thrombolysis. *In vitro* human thrombi were incubated with nanoparticles at different concentrations at room temperature for 1 h. The weight of glass vials was measured before and after the experiment, and the initial and final temperatures were also recorded with a thermal camera (FLIR, US). The thrombi were irradiated with an 808 nm infrared laser. After the laser exposure, the liquid remaining of the lysis was discarded and the clot mass loss was calculated for each thrombus. The mass loss percentage was normalized against that of the thrombus with no treatment or PBS.

2.5. Photothermal Cancer Cell Treatment. Human breast cancer cells (MDA-MB-231) were incubated with different concentrations of the nanoparticles. After 1 day, the cells were washed with PBS and irradiated with an 808 nm infrared laser. Cell viability was evaluated using PrestoBlue cell viability reagent as described above.

2.6. Histology and *In Vivo* Biodistribution. Five-month-old C57BL/6 wild-type mice (Animal Resources Centre, ARC, Western Australia) were injected with the nanoparticles at a dose of 3.2 mg/kg mouse. The mice were sacrificed at 1, 3, and 7 days post injection and organs (heart, lung, kidney, liver, spleen) were collected for analysis.

https://doi.org/10.1021/acsanm.1c01571
ACS Appl. Nano Mater. XXXX, XXX, XXX−XXX

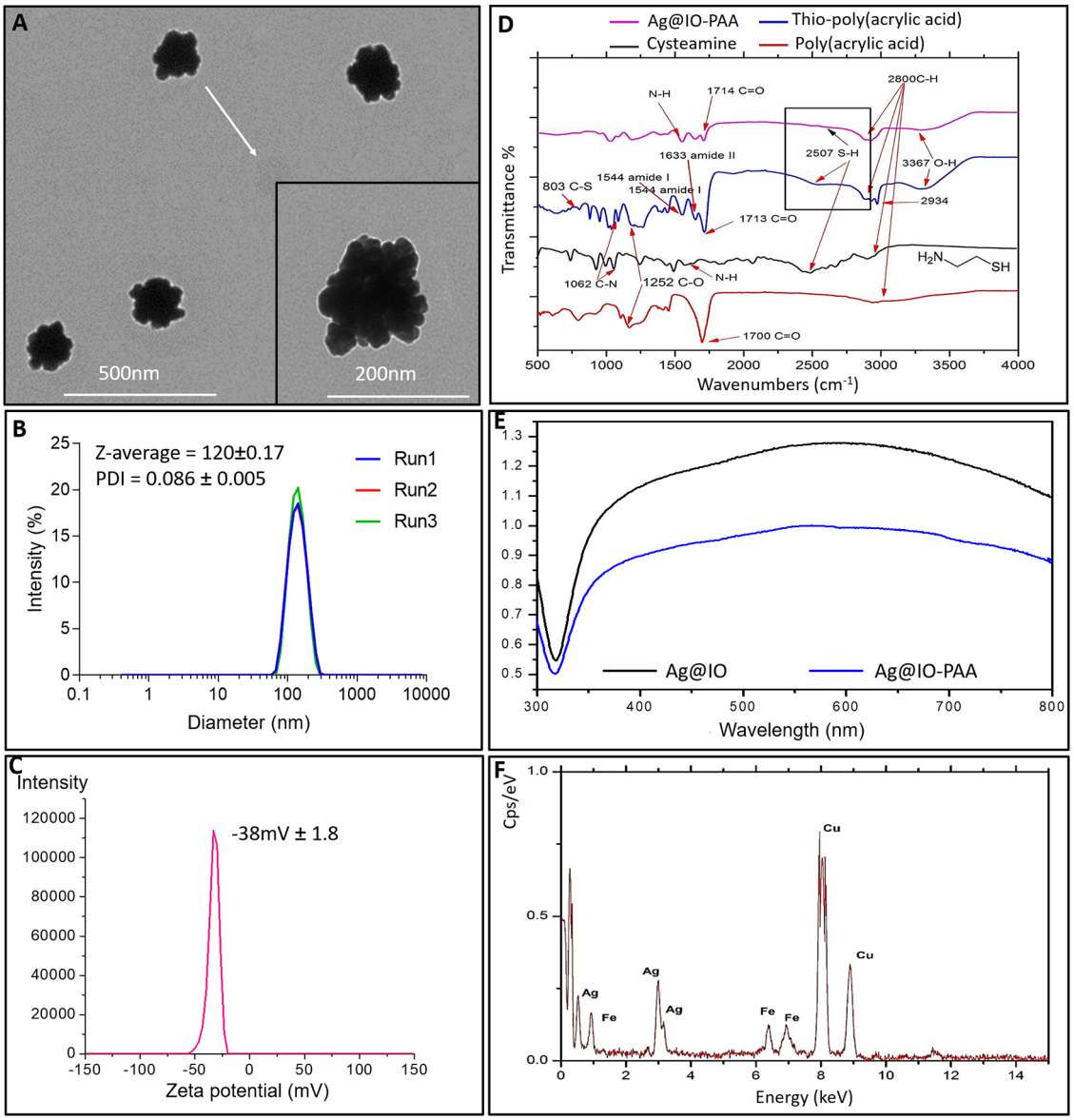

Figure 1. Characterization of Ag@IO-PAA. (A) TEM image of Ag@IO-PAA nano-popcorns (scale bar = 500 and 200 nm). (B) Size distribution and (C) ZP of the nano-popcorns obtained from DLS. (D) FTIR spectra of Ag@IO-PAA, PAA-SH, PAA, and cysteamine (4000−500 cm^{-1} region). (E) Absorption spectra of Ag@IO and Ag@IO-PAA. (F) Energy-dispersive spectrum (EDS) of the nano-popcorns.

For histology analysis, the samples were cut into 10 μm thick cross sections and stained with hematoxylin and eosin (H&E). For biodistribution analysis, the organs were dissolved in aqua regia for 3 days at room temperature. The lysis solutions were centrifuged to remove all debris and then diluted 1:10 for inductively coupled plasma mass spectrometry (ICP-MS) analysis. ICP-MS was used to detect the content of Ag in the organs.

3. RESULTS AND DISCUSSION

3.1. Optimization and Characterization of Ag@IO-PAA Nano-Popcorns. The characteristics of the IONPs in terms of size, surface charge, morphology are presented in Figure S1. The size distribution of the IONPs in terms of number (mean = 20 nm) and intensity (mean = 38 nm) shows low polydispersity (PDI = 0.176). Transmission electron microscopy (TEM) also confirms the small size and size uniformity of the IONPs. The surface charge of the IONPs was highly negative (ZP = −42 mV). The cluster morphology in the TEM image of IONPs (Figure S1-D) is attributed to high surface energy and small size, leading to aggregation in the drying step. Such clusters and aggregation are dissociated in the IONPs dispersion as there is no peak corresponding to large-size clusters in the dynamic light scattering (DLS) graphs.

To achieve uniform nano-popcorn morphology with absorbance in the NIR and visible regions, the process of silver coating was optimized. The HDX was used as a reducing agent along with trisodium citrate as a capping agent. Upon silver deposition on IONPs as seeds, the particle size was increased (Table S1). The deposition mechanism relies on the nucleation and growth of Ag^{+} by reduction on the surface of IONP seeds. Different ratios of silver to iron were tested when the concentrations of HDX (reducing agent) and trisodium citrate (capping agent) were kept constant at 2 μL and 150 μL, respectively. As the Ag^{+}/Fe ratio increased, the absorbance curve shifted toward the NIR region (Figure S2). At the ratio of 0.2, the absorbance peak is around 400 nm, while it was

https://doi.org/10.1021/acsanm.1c01571
ACS Appl. Nano Mater. XXXX, XXX, XXX−XXX

shifted to visible and NIR regions at the ratio of 1. The popcorn morphology of the prepared nanoparticles is due to the combination effects of the nucleation and growth by the reduction of the Ag^+ on an iron oxide nanocluster and then on the Ag^0 surface. The nonspherical shape of the nanocluster core with knobby surface also contributes to a highly asymmetric geometry for the Ag coatings. Moreover, HDX as the reducing agent has an important role to play in the nucleation and catalytic growth of the silver ions on the IONPs' surface, and therefore in developing knobby and bumpy morphology. The adsorption of slow reacting citrate on the silver possibly provides the preferred direction for the further growth of the silver. The influence of HDX is to expedite the reduction of silver ion on the surface of active sites. The rapid reduction may be due to the effect of this preferential Ag+ absorption as produces asymmetricity.[51−53] It was found that as the amount of HDX increases (ranging from 2 to 20 μL), the absorbance peak is broadened, shifted to the IR range, and intensified (Figure S3), which can be attributed to the development of unique surface morphology as the particle shape and morphology affect the plasmonic absorbance strongly.[54] Figure S4 shows the morphology of the silver/iron oxide hybrid nanoparticles as the amount of HDX increased. The optimum HDX and TSC concentrations as well as the Ag^+/Fe ratio were found to be 20 μL, 150 μL, and 1, respectively.

The magnetic nanoclusters have a size of around 38 nm (Figure S1). Upon silver coating, the size increased to around 105 nm (Table S1). Further PAA coating resulted in an Ag@IO-PAA nanoparticle with the size of 120 nm (Table S1). ICP results showed that the Ag/Fe mass ratio of the nano-popcorn is around 106. The morphology of the optimized Ag@IO-PAA was demonstrated by TEM, showing irregular, nano-popcorn shape and good uniformity (Figure 1A). The nano-popcorns had a narrow size distribution (PDI = 0.086) with a hydrodynamic size of 120 ± 0.17 nm and a highly negative ZP of −38 ± 1.8 mV (Figure 1B,C). To verify the coating of PAA on the surface of Ag@IO, Fourier transform infrared (FTIR) spectra were recorded (Figure 1D). Since PAA was modified with cysteamine to introduce thiol groups, which have strong bonding to silver surface,[55] a weak characteristic peak at around 2507 cm^{-1} attributed to S−H stretching was detected in thiolated PAA spectrum. The presence of the absorption bands at 1544 and 1633 cm^{-1} which are, respectively, attributed to amide I and amide II bands further confirms the successful thiolation of PAA. The former and the latter are ascribed to C═O stretching vibration and N−H bending vibration in the amide bond, respectively.[56] In the FTIR spectrum of Ag@IO-PAA, the S−H stretching disappeared, indicating that Ag@IO nano-popcorns were stabilized by thiolated PAA.

The specific optical feature of Ag@IO and Ag@IO-PAA, which is usually the SPR, was depicted by UV−vis−NIR spectra (Figure 1E). As mentioned previously, there are no nanosized silver/iron oxide hybrid particles having SPR in the NIR window so far. Therefore, the purpose of our study is to tune the SPR effect of Ag@IO to the desirable NIR range for optimal biomedical applications. To shift the SPR peak of the nanoparticles, there are several ways such as change of the coating material, surface modification, surface charge, inter-particle interaction, as well as shape tuning.[57,58] Regarding the latter, nanoparticles with a variety of morphologies from spherical, rod, cube, shell to cage, triangle, and star have been synthesized. It has been found that nanoparticles with elongated (e.g., nanorod) or asymmetrical (e.g., nano-star/nano-popcorn) shapes tend to shift the SPR to NIR.[59−61] As can be seen in Figure 1E, the prepared Ag@IO with nano-popcorn morphology exhibited a broad absorption spectrum shifted up to the NIR region. The absorption spectrum of Ag@IO-PAA was similar to that of Ag@IO, suggesting that the PAA coating layer had no effect on the SPR of the nano-popcorns. In Figure 1F, the EDS spectrum taken from Ag@IO-PAA showed Ag and Fe peaks, which confirms the presence of both Ag and Fe in the nanoparticles. Moreover, the broad and shifted absorption spectrum proves the Ag growth on the surface of IONPs.

Ag@IO-PAA was found to be relatively stable in different physiological solutions after 2 weeks. Figure S5 shows that these nanoparticles had good stability in three different media (PBS, RPMI, DMEM). Very small agglomeration was noted in RPMI and DMEM solution.

The Ag@IO-PAA nano-popcorns at different iron concentrations prepared in phantoms were investigated for MRI signals. As the iron concentration increased in the nano-popcorns, the signal intensity gradually decreased in comparison to the control phantom (Figure 2A). At the same Fe concentration, the longer the echo time (TE), the greater the signal loss. Imaging parameters, such as echo and repetition time (TE and TR), are used to provide different weightings within the image. They can be optimized to best visualize the object. As can be seen in this study, at the same TR, different TE provided different contrast effects. The relaxation rate, $R_2 = 1/T_2$, was linearly proportional to the iron concentration of Ag@IO-PAA (Figure 2B). From the plot in Figure 2B, transverse relaxivity (r_2) of Ag@IO-PAA nano-popcorns was 46.2 mM^{-1} s^{-1} and hence can be utilized as a reliable MRI contrast agent. The reduced r_2 of Ag@IO-PAA compared to IONP (r_2 = 164 mM^{-1} s^{-1}, Figure S6) could be due to the silver coating and the PAA layer.

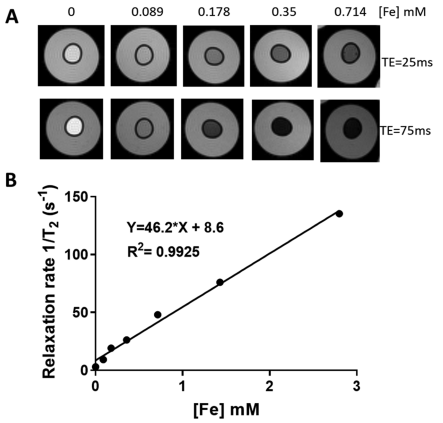

Figure 2. MRI of Ag@IO-PAA. (A) T_2-weighted images of the nano-popcorns prepared in phantoms at different concentrations, acquired using a 9.4 T MRI scanner at different TE. (B) Plot of relaxation rates $1/T_2$ versus Fe concentrations of Ag@IO-PAA.

3.2. *In Vitro* MRI of Ag@IO-PAA Nano-Popcorns in Macrophages, Cancer Cells, and Thrombus. Subsequently, *in vitro* MRI images of macrophages J774A.1 and cancer cells MDA-MB-231 in the presence of nano-popcorns were examined. The cells were treated with Ag@IO-PAA at concentrations of 0, 0.1, and 0.2 mg/mL for 12 h, followed by

https://doi.org/10.1021/acsanm.1c01571
ACS Appl. Nano Mater. XXXX, XXX, XXX−XXX

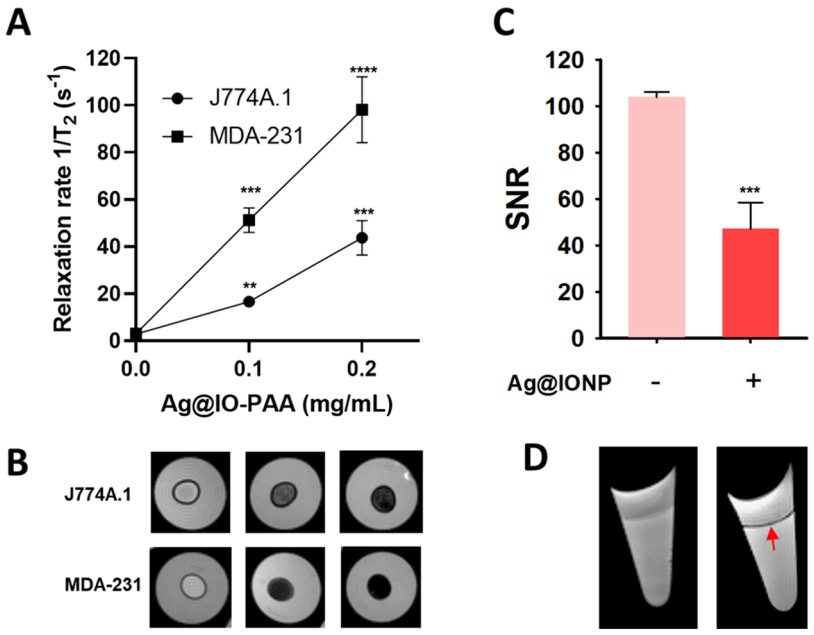

Figure 3. *In vitro* cells and thrombus MRI. (A) Graph plotting relaxation rates $1/T_2$ and (B) T_2-weighted images of macrophages (J774A.1) and cancer cells (MDA-MB-231) incubated with Ag@IO-PAA (0, 0.1, 0.2 mg/mL) for 12 h and resuspended in 1% agarose gel under a 9.4 T MRI scanner. (C) Graph plotting T_2-weighted signal-to-noise-ratio (SNR) of thrombus edge from thrombus only (−) and thrombus incubated with Ag@IO-PAA-RGD (+) (named as Ag@IONP in the graph). (D) T_2-weighted images of thrombus (−) and thrombus incubated with Ag@IONP (+). $N = 3$, $^{**}P < 0.01$, $^{***}P < 0.001$, $^{****}P < 0.0001$ versus controls (samples without the nanoparticles).

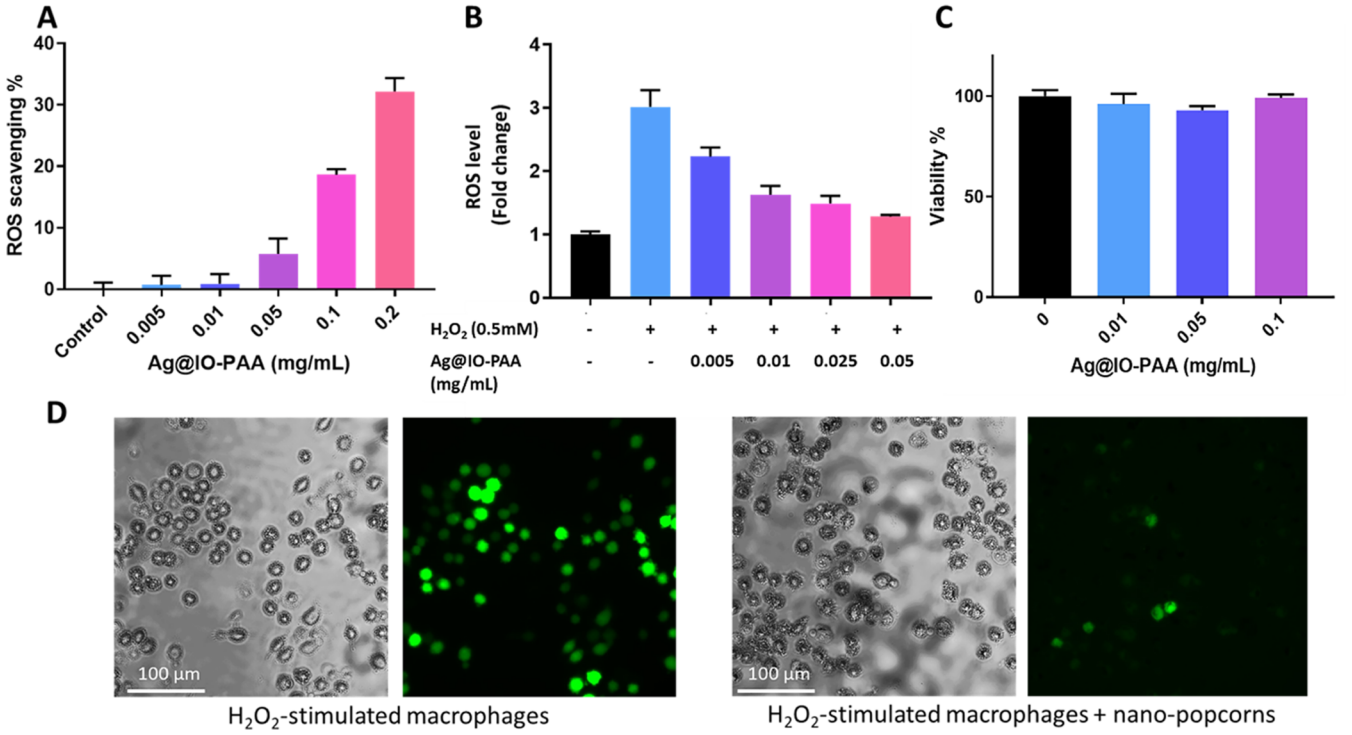

Figure 4. ROS scavenging capability of Ag@IO-PAA nano-popcorns. (A) Different concentrations of the nano-popcorns were assessed for the ROS scavenging ability in the H_2O_2-HRP-ABTS system. Treatment group without nano-popcorns was considered as control with 0% ROS scavenging. (B) Macrophages treated with different concentrations of the nano-popcorns followed by H_2O_2 stimulation were assessed for the ROS level. Macrophages without nano-popcorns treatment and H_2O_2 stimulation were considered as control with ROS level = 1. (C) Cytotoxicity of the nano-popcorns at different concentrations to macrophages. (D) Bright-field and fluorescence images of H_2O_2-stimulated macrophages (left) and H_2O_2 macrophages after nano-popcorns treatment at the highest concentration (0.05 mg/mL) (right) (scale bar = 100 μm). $N = 3$.

collection and even suspension in 1% agarose gel for MRI scan. As shown in Figure 3A,B, both macrophages and cancer cells incubated with the nano-popcorns could be easily detected under a 9.4 T MRI scanner by a significant signal loss in T_2-weighted images due to a significantly higher R_2 in comparison

https://doi.org/10.1021/acsanm.1c01571
ACS Appl. Nano Mater. XXXX, XXX, XXX−XXX

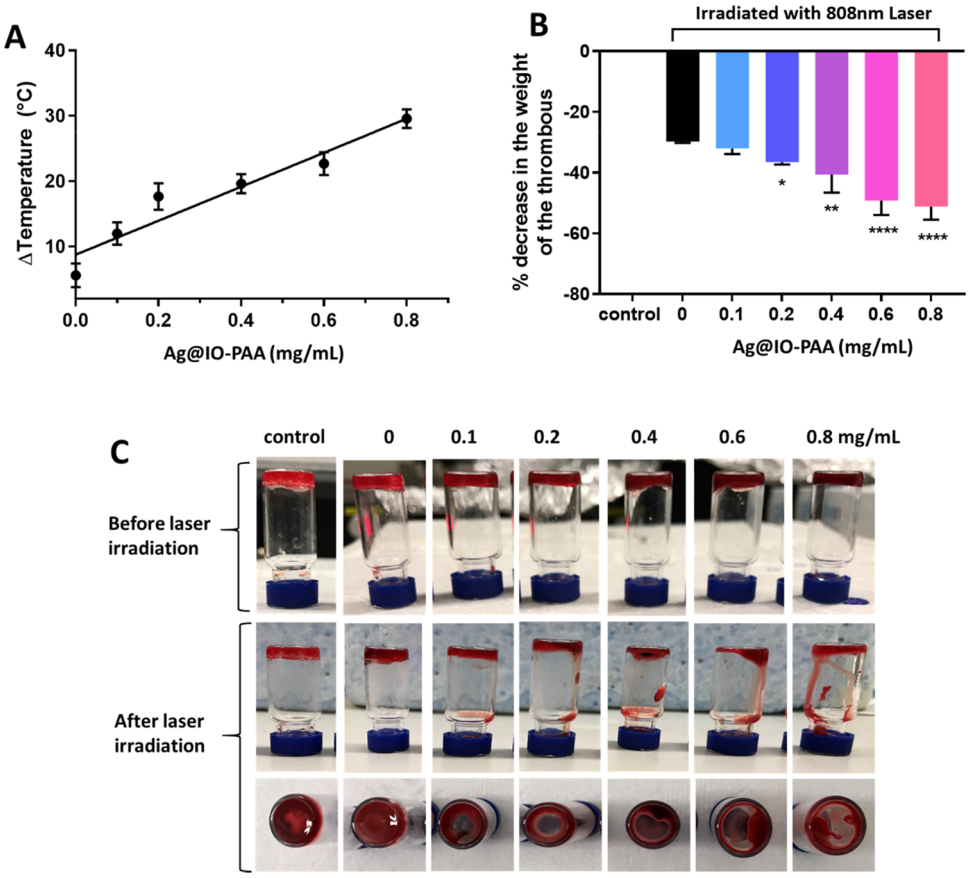

Figure 5. *In vitro* photothermal thrombolytic effect of Ag@IO-PAA. (A) Plot of temperature change over 120 s versus different concentrations of the nano-popcorns upon the irradiation of an 808 nm infrared laser. (B) Photothermal thrombolytic effect of the nano-popcorns at different concentrations irradiated with an 808 nm infrared laser. (C) Images showing the thrombus without laser irradiation (control) and thrombus incubated with different nano-popcorn concentrations before and after irradiation with an 808 nm infrared laser. $N = 3$, $^{*}P < 0.05$, $^{**}P < 0.01$, $^{***}P < 0.001$, $^{****}P < 0.0001$ versus control (thrombus without any treatments).

to the blank cell control. Relaxation rates of the blank macrophage control and blank cancer cell control were similar.

Interestingly, Figure 3A,B also demonstrates that cancer cells exhibited higher R_2 than macrophages, corresponding to the more hypointense T_2-weighted image, which is most likely due to different uptake levels of the nanoparticles in different cell types.[62] These results revealed that Ag@IO-PAA can be sequestered within cells for *in vivo* labeling and tracking of both macrophages and cancer cells. The high uptake of the Ag@IO-PAA in MDA-MB-231 cancer cells also shows that the nano-popcorns could be good candidates for breast tumor or cancer cell detection and therapy.

Besides the cells, *in vitro* MRI signal of thrombus incubated with the nano-popcorns was also evaluated. RGD peptide was used to target the NPs to thrombus by binding to activated platelets. Platelets are major components of a thrombus. Figure 3C shows that T_2-signal of thrombus incubated with targeting peptide-labeled nanoparticles (Ag@IO-PAA-RGD, named as Ag@IONP+ in the graph) was diminished due to the presence of the nano-popcorns on the surface of the thrombus. As a result, a thin and black ring on top of the thrombus was detected in T_2-weighted image, indicated by red arrow while thrombus without nano-popcorns did not have any obvious black ring (Figure 3D). T_2-signal diminishment only occurred on the surface of thrombus imaged in the form of a thin and black ring as the nano-popcorns were incubated and presented only on the top of the thrombus. Overall, Ag@IO-PAA-RGD showed excellent MRI contrast effect on thrombus in T_2-weighted image, implying that these nano-popcorns can act as a potential imaging agent for thrombus detection.

3.3. ROS Scavenging Capability of Ag@IO-PAA Nano-Popcorns. H_2O_2-HRP-ABTS system was used to investigate the ROS scavenging capability of Ag@IO-PAA where the nano-popcorns were incubated with H_2O_2 in the presence of HRP as a catalyst for the oxidization of ABTS. The reduction in the absorbance of the sample solution was inversely proportional to the % ROS scavenging. The significant increase in the anti-ROS effect compared to the control was only observed when using nano-popcorns at the concentration of 0.05 mg/mL and above (Figure 4A). At 0.2 mg/mL, the ROS level in the solution was scavenged up to 33%, which revealed a relatively good anti-ROS effect of the nano-popcorns in buffer solution.

ROS scavenging activity of the nano-popcorns was further tested in activated macrophages since these cells release excessive ROS upon the phagocytosis or immune response to the stimulation of various agents.[63] After stimulating macrophages with 0.5 mM H_2O_2 for 15 min, the ROS level was 3-fold higher than that of the control cells (Figure 4B). Results from Figure 4B indicate a significant suppression of ROS upon treatment of activated macrophages with Ag@IO-PAA at 0.005 mg/mL. The level of ROS in activated macrophages incubated with nano-popcorns at the concentration of 0.05 mg/mL was suppressed to 1.3-fold compared to the normal. DCFDA was

https://doi.org/10.1021/acsanm.1c01571
ACS Appl. Nano Mater. XXXX, XXX, XXX−XXX

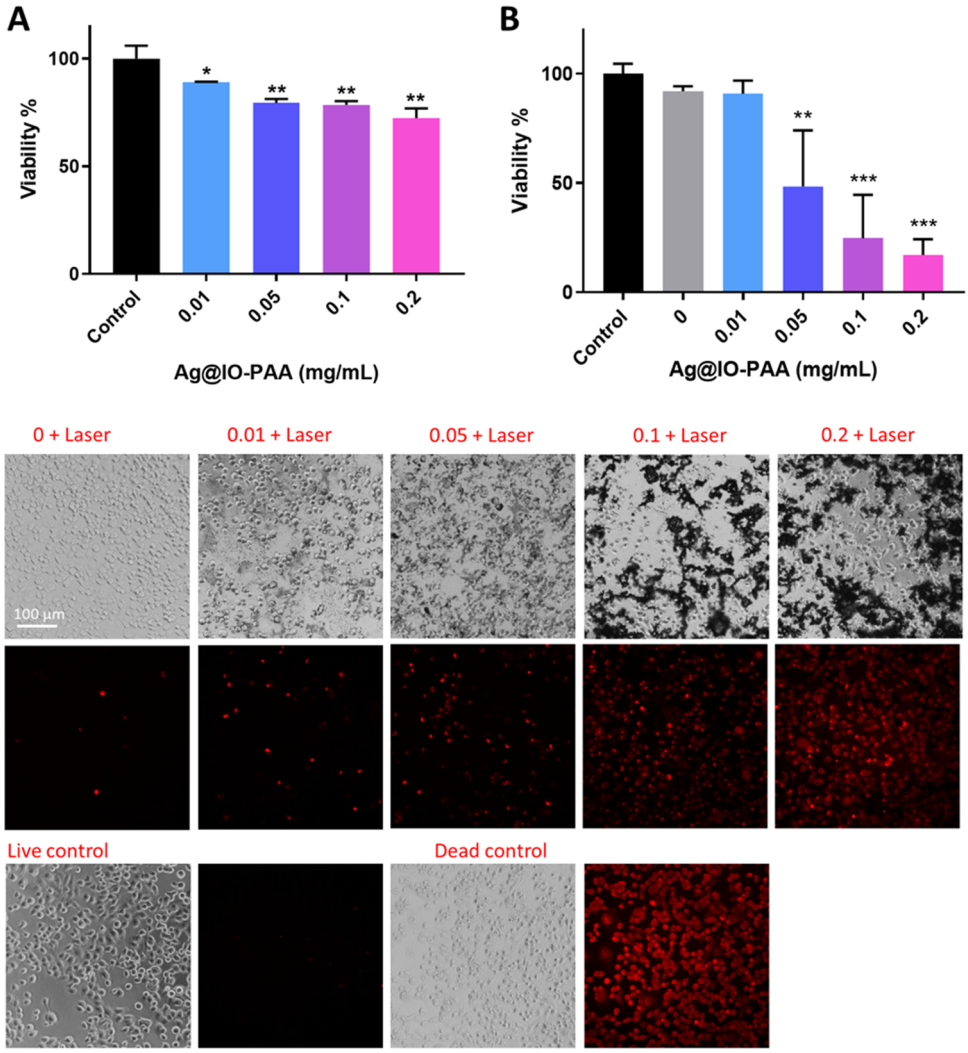

Figure 6. *In vitro* cancer cell experiments. (A) Viability of MDA-MB-231 cells incubated 24 h with different concentrations of Ag@IO-PAA nano-popcorns. (B) Photothermal treatment of MDA-MB-231 cells by incubating cells with different concentrations of Ag@IO-PAA nano-popcorns for 24 h followed by the irradiation of 808 nm infrared laser (1.59 W/cm^2, 2 min). (C) Bright-field and fluorescence images showing the viability of cancer cells incubated with different concentrations of the nano-popcorns after photothermal treatment (scale bar = 100 μm). MDA-MB-231 cells were treated with ethidium homodimer-1 fluorescence dye (1 μM) for 30 min to detect dead cells (red fluorescent cells). $N = 3$, * $P < 0.05$, ** $P < 0.01$, *** $P < 0.001$.

employed to evaluate ROS level in macrophages. DCFDA is deacetylated by cellular esterases to a nonfluorescent compound, which is later oxidized by ROS into 2′,7′-dichlorofluorescein (DCF). DCF is highly fluorescent and can be detected by a spectrometer or a fluorescence microscope. Figure 4C shows fluorescence images of the cells, which represent intracellular ROS levels. As expected, the fluorescence emission was hardly detected inside the cells treated with the nano-popcorns (0.05 mg/mL) in comparison with the bright fluorescence emission in the cells without nano-popcorns incubation. These results demonstrated that Ag@IO-PAA nano-popcorns at the concentration of 0.005−0.05 mg/mL can act as a ROS scavenger to effectively downregulate the ROS level in macrophages. However, it is important to note that the ROS scavenging ability of silver-based NPs depends on the amount of the NPs used since at a high concentration, the NPs can exert high toxicity to cells and trigger ROS generation as reported in previous studies.[32,33] Aside from that, the toxicity of silver-based NPs is also dependent on particle size, coating material, and morphology structure that can lead to more ROS production.[64] Therefore, further investigations for finding a safe and optimal concentration range for anti-ROS activity are encouraged. In this study, the tested concentration range of Ag@IO-PAA nano-popcorns showed no significant toxicity to the macrophages (Figure 4D).

3.4. Photothermal Thrombolytic Effect of Ag@IO-PAA Nano-Popcorns. Application of photothermal therapy for thrombosis is still relatively new. Figure 1E shows that Ag@IO-PAA nano-popcorns possess a strong and broad SPR up to the NIR region, which was predicted to benefit the light-to-heat conversion using the NIR laser. The photothermal conversion performance of Ag@IO-PAA was evaluated by exposing various concentrations of the nano-popcorns (0−0.8 mg/mL) to an 808 nm infrared laser (1.59 W/cm^2). After 120 s, the nano-popcorns exhibited good photothermal conversion effect in a concentration-dependent manner (Figure 5A). The temperature of the nano-popcorns solution at 0.2 mg/mL increased by nearly 20 °C after the laser irradiation. At the highest nano-popcorns concentration (0.8 mg/mL), the temperature increment can be up to 30 °C.

https://doi.org/10.1021/acsanm.1c01571
ACS Appl. Nano Mater. XXXX, XXX, XXX−XXX

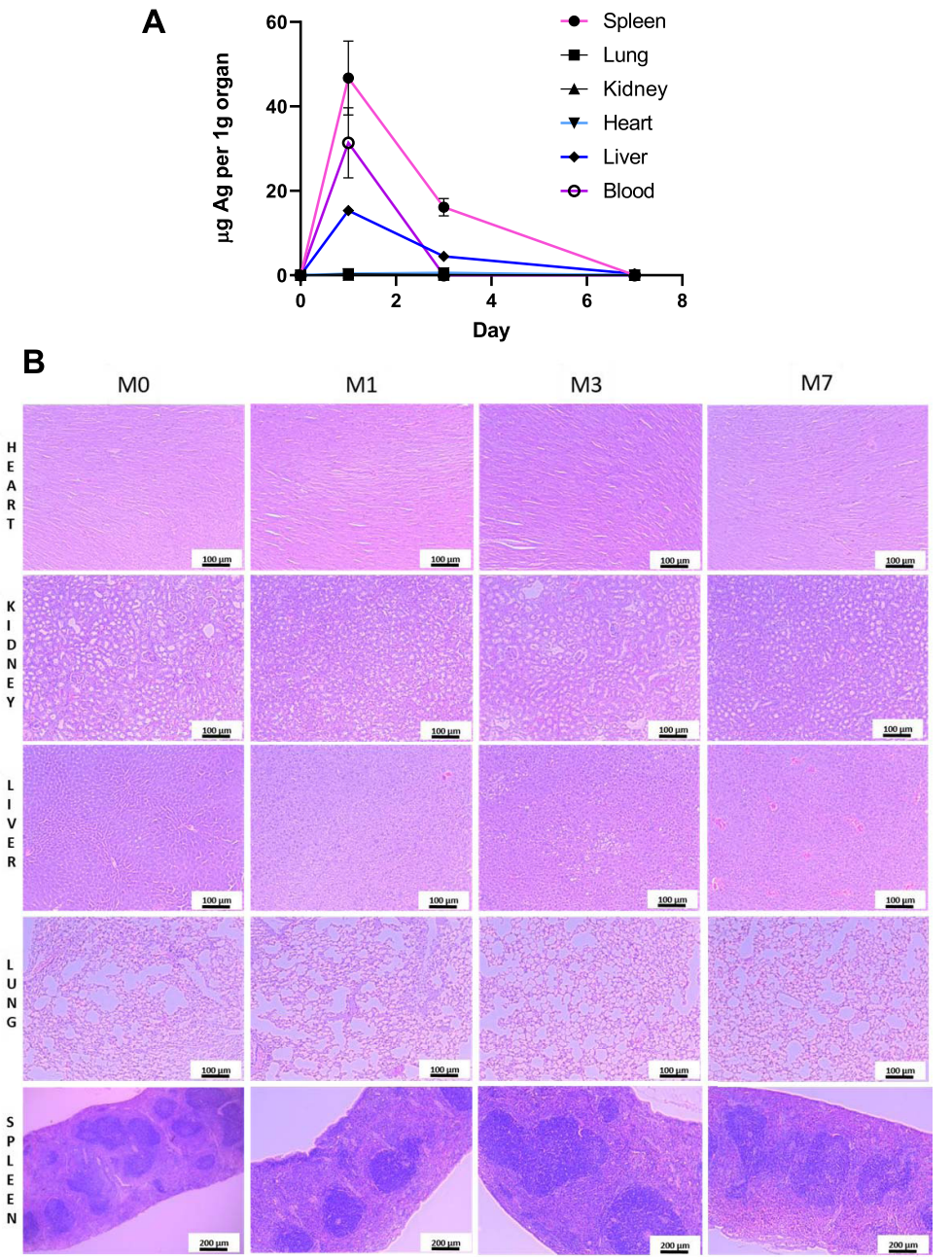

Figure 7. Biodistribution (A) and histopathology effects of Ag@IO-PAA (B). H&E stained sections of heart (100×), kidney (100×), liver (100×), lung (100×), and spleen (40×) of treated Ag@IO-PAA mice. M1, M3, and M7 refer to mice organs on days 1, 3, and 7 after administration of the nanoparticles, respectively. M0 refers to the control. $N = 3$. Scale bar: 100 μm for heart, kidney, liver, lung; 200 μm for spleen.

After confirming the efficient photothermal conversion ability, the nano-popcorns were added to the clots followed by the irradiation of NIR laser for 120 s to evaluate their photothermal thrombolytic effect. The effect of 100 μL of nano-popcorns at different concentrations ranging from 0 to 0.8 mg/mL on the clot was evaluated (Figure 5B). These concentrations are equal to 0, 0.09, 0.18, 0.36, 0.54, and 0.72 μg nano-popcorns per 1 mg clot. The effect was expressed in terms of percentage decrease in thrombus mass. Thrombus without nano-popcorns and laser treatment was set as the control. Under the continuous irradiation of 808 nm laser, the thrombus mass loss was around 30% (Figure 5B). Near-infrared laser can cause temperature increase and has photothermal interactions with the clot's components, which could weaken the clot matrix for the lysis. Near-infrared light action on RBCs causes dehydration of proteins, quaternary transitions in hemoglobin, and alterations of membrane fluidity and membrane potential.[65] This could be the reason for the reduction of thrombus weight by the irradiation of an 808 nm laser only. The thrombus treated with low concentration (0.1 mg/mL) of the nano-popcorns showed negligible improvement in reducing the thrombus mass after laser irradiation. However, a significant thrombolytic effect was observed when the nano-popcorn concentration of 0.2 mg/mL and above was utilized, which is in agreement with the photothermal conversion performance result (Figure 5A). Approximately 50% of the thrombus was lysed at 0.8 mg/mL of the nano-

https://doi.org/10.1021/acsanm.1c01571
ACS Appl. Nano Mater. XXXX, XXX, XXX−XXX

popcorns. The lysis of the thrombus was visualized (Figure 5C).

The nano-popcorns showed negligible hemolysis at all tested concentrations (0.025−0.8 mg/mL) after 4 and 24 h of incubation with diluted red blood cells (Figure S7). However, at the concentration of 0.8 mg/mL, Ag@IO-PAA could cause damage to the normal cell line. Therefore, further optimization of the nano-popcorns with RGD peptide or other targeting ligands to enhance targeting and accumulation of the nano-popcorns at the clot will help reduce the dose required for thrombolysis and thus potentially reduce their toxicity side effect. Overall, Ag@IO-PAA nano-popcorns demonstrated an excellent photothermal thrombolytic effect, which is promising for the photothermal treatment of thrombosis.

In this proof-of-concept study, only one long cycle of continuous laser irradiation at 1.59 W/cm^2 for 2 min was employed to demonstrate the thrombolysis capability of the nano-popcorns. Further studies will be conducted to optimize the irradiation condition so that the best thrombolysis effect can be achieved with minimal temperature increase to avoid or minimize thermal damage to surrounding tissues. Parameters such as laser power, time, and irradiation cycle number will be varied and investigated.

3.5. *In Vitro* Cytotoxicity and Photothermal Treatment in Cancer Cells. The assessment of cytotoxicity of Ag@IO-PAA nano-popcorns was conducted with MDA-MB-231 breast cancer cells. A minimal decrease in cell viability (5−20%) was observed when the cells were incubated with 0.01−0.2 mg/mL of the nano-popcorns for 24 h (Figure 6A). Thereafter, MDA-MB-231 cancer cells incubated with nano-popcorns at the same concentrations were exposed to an 808 nm laser for 2 min to evaluate the photothermal treatment efficiency (Figure 6B). The laser irradiation at 808 nm did not cause toxicity on the cancer cells in comparison to the control group (cells without any treatment). In contrast, when laser irradiation was applied on the cells treated with the nano-popcorns, a drastic decrease in the breast cancer cell viability was observed (less than 50% viable cells at nano-popcorn concentrations from 0.05 to 0.2 mg/mL). Ethidium homodimer-1 (EthD-1) was also used to qualitatively determine cell viability after treatment, and dead cells (indicated by red fluorescence) are depicted in Figure 6C. EthD-1 is a high-affinity nucleic acid stain that is weakly fluorescent until bound to DNA and emits red fluorescence. Dead cells have disrupted membrane, and thus can be stained by EthD-1. These encouraging results give insight into the potential of Ag@IO-PAA nano-popcorns as an effective NIR photothermal treatment strategy for anticancer therapy.

3.6. *In Vivo* Biodistribution and Histological Study. The biodistribution of Ag@IO-PAA in C57BL/6 mice was evaluated over a period of 7 days. ICP was employed to determine Ag level in each organ over time. Ag level represents the level of the nanomaterials in the organs. Figure 7A shows that Ag@IO-PAA accumulated mostly in the spleens and livers on day 1 post-injection of the materials and then declined to baseline level on day 7 post-injection. The Ag or nanomaterial levels in kidneys, lungs, and hearts were negligible. The particles remained significantly high in the blood circulation on day 1 and completely cleared off on day 3.

To detect the biocompatibility of Ag@IO-PAA, we sectioned vital organs from the treated mice. The tissue sections were stained, and then microstructural changes of the tissues were observed by an optical microscope. Histological images of organs from treated animals after 1, 3, and 7 days post-injection of Ag@IO-PAA (M1, M3, M7) exhibited insignificant pathological changes. The H&E stained sections of vital organs show no apparent tissue damage, inflammation, or lesions from exposure with the nanoparticles in comparison with the control (M0) (Figure 7B). There was no abnormal evidence and inflammatory cell infiltration in organs after treatment. These findings demonstrated that Ag@IO-PAA at a dosage of 3.2 mg/kg in mouse poses no significant signs of toxicity.

CONCLUSIONS

For the first time, the multifunctional theranostic Ag@IO-PAA nano-popcorns were successfully synthesized and SPR was tuned to the desirable NIR range. These nano-popcorns are potential materials for the diagnosis and treatment of diseases related to ROS, cancer, and thrombosis. Given this advantage, the obtained nano-popcorns featured an excellent photothermal conversion performance upon irradiation of an 808 nm NIR laser and are highly promising for the photothermal treatment of both thrombosis and anticancer therapy. Our results also revealed that Ag@IO-PAA nano-popcorns possess efficient anti-ROS ability in buffer solution and acted as scavengers to downregulate the ROS level in macrophages. Apart from the therapeutic capabilities, this nano-popcorn system could be a potential MRI imaging agent as well. The *in vitro* MRI study indicated that the nano-popcorns have excellent contrast effect after being sequestered within cells (macrophages and cancer cells) or positioned on the surface of the thrombus, which could provide a noninvasive labeling and tracking of inflammation (macrophage-rich areas), cancer cells (tumor), and thrombus. Our results indicate that the developed nano-popcorn has great potential to perform as a theranostic material for ROS-related and inflammatory diseases, cancers, and thrombosis. In addition, our nano-popcorns demonstrated negligible toxicity in cells (macrophages and breast cancer cell) and had no evidence of inflammatory cell infiltration in organs after treatment in histological investigation. The nano-popcorns were cleared off and not retained in the mouse organs after 7 days. Further modification of our multifunctional nano-popcorns with either peptides or antibodies targeting ROS-related cells, cancer cells, and/or thrombus will create an effective agent for monitoring and targeted strategy for the treatment of various types of diseases. In future studies, we will test the performance of these nano-popcorns in mouse models of thrombosis and cancers.

ASSOCIATED CONTENT

Supporting Information

The Supporting Information is available free of charge at https://pubs.acs.org/doi/10.1021/acsanm.1c01571.

Materials, methods, and additional/supporting results: characterization of iron oxide nanoparticles; DLS data of coated and bare nanoparticles; optimization of the nano-popcorns; stability of the nano-popcorns in different buffers; MRI data of iron oxide nanoparticles; and hemocompatibility data (PDF)

AUTHOR INFORMATION

Corresponding Author

Hang T. Ta − *Queensland Micro- and Nanotechnology Centre, Griffith University, Brisbane 4111, Australia; School of*

https://doi.org/10.1021/acsanm.1c01571
ACS Appl. Nano Mater. XXXX, XXX, XXX−XXX

Environment and Science, Griffith University, Brisbane 4111, Australia; Australian Institute for Bioengineering and Nanotechnology, University of Queensland, Brisbane 4072, Australia; orcid.org/0000-0003-1188-0472; Email: h.ta@griffith.edu.au

Authors

Ateeque ur Rehman − *Queensland Micro- and Nanotechnology Centre, Griffith University, Brisbane 4111, Australia; Department of Physics, The Islamia University of Bahawalpur, Bahawalpur, Punjab 63100, Pakistan*

Yuao Wu − *Queensland Micro- and Nanotechnology Centre, Griffith University, Brisbane 4111, Australia; Australian Institute for Bioengineering and Nanotechnology, University of Queensland, Brisbane 4072, Australia*

Huong D. N. Tran − *Queensland Micro- and Nanotechnology Centre, Griffith University, Brisbane 4111, Australia; Australian Institute for Bioengineering and Nanotechnology, University of Queensland, Brisbane 4072, Australia*

Karla Vazquez-Prada − *Queensland Micro- and Nanotechnology Centre, Griffith University, Brisbane 4111, Australia; Australian Institute for Bioengineering and Nanotechnology, University of Queensland, Brisbane 4072, Australia*

Yajun Liu − *Australian Institute for Bioengineering and Nanotechnology, University of Queensland, Brisbane 4072, Australia*

Hossein Adelnia − *Queensland Micro- and Nanotechnology Centre, Griffith University, Brisbane 4111, Australia; Australian Institute for Bioengineering and Nanotechnology, University of Queensland, Brisbane 4072, Australia*

Nyoman D. Kurniawan − *Centre for Advanced Imaging, University of Queensland, Brisbane 4072, Australia*

Muhammad Naeem Anjum − *Department of Physics, The Islamia University of Bahawalpur, Bahawalpur, Punjab 63100, Pakistan*

Shehzahdi S. Moonshi − *Queensland Micro- and Nanotechnology Centre, Griffith University, Brisbane 4111, Australia*

Complete contact information is available at: https://pubs.acs.org/10.1021/acsanm.1c01571

Author Contributions

#Y.W. and H.D.N.T. equally contributed to this work.

Author Contributions

A.R. synthesized, characterized the nanoparticles, and performed photothermal assays. Y.W. performed TEM, EDS, and most cell-based assays. H.D.N.T. wrote and revised the manuscript. K.V.P. performed hemocompatibility assay and analyzed histology data. Y.L. performed cell-based ROS assays. M.N.A. provided advices and contributed to data analysis. N.K. performed MRI of iron oxide nanoparticles. H.T.T. provided guidance, supervised the whole project, performed MRI, carried out the *in vivo* study, and performed data analysis. H.T.T., S.S.M., K.V.P., and H.A. contributed to writing and revising the manuscript

Notes

The authors declare no competing financial interest.

■ ACKNOWLEDGMENTS

This work was funded by National Health and Medical Research Council (H.T.T.: APP1037310, APP1182347, APP2002827), Heart Foundation (H.T.T.: 102761), Pakistan Higher Education Commission (A.R.: International Research Support Initiative Program Scholarship), and the University of Queensland (H.D.N.T., K.V.P., H.A.: Research Training Scholarship). The authors would like to acknowledge the Australian National Fabrication Facility (Queensland Node) and National Imaging Facility, Centre for Advanced Imaging at the University of Queensland for access to key items of equipment.

■ REFERENCES

(1) Rizzo, L. Y.; Theek, B.; Storm, G.; Kiessling, F.; Lammers, T. Recent progress in nanomedicine: therapeutic, diagnostic and theranostic applications. *Curr. Opin. Biotechnol.* **2013**, *24*, 1159−1166.

(2) Sumer, B.; Gao, J. Theranostic nanomedicine for cancer. *Nanomedicine* **2008**, *3*, 137−140.

(3) Kim, T. H.; Lee, S.; Chen, X. Nanotheranostics for personalized medicine. *Expert Rev. Mol. Diagn.* **2013**, *13*, 257−269.

(4) Zavaleta, C.; Ho, D.; Chung, E. J. Theranostic nanoparticles for tracking and monitoring disease state. *SLAS Technol.* **2018**, *23*, 281−293.

(5) Vogenberg, F. R.; Isaacson Barash, C.; Pursel, M. Personalized medicine: part 1: evolution and development into theranostics. *Pharm. Ther.* **2010**, *35*, 560−576.

(6) Ta, H. T.; Li, Z.; Hagemeyer, C. E.; Cowin, G.; Zhang, S.; Palasubramaniam, J.; Alt, K.; Wang, X.; Peter, K.; Whittaker, A. K. Molecular imaging of activated platelets via antibody-targeted ultra-small iron oxide nanoparticles displaying unique dual MRI contrast. *Biomaterials* **2017**, *134*, 31−42.

(7) Dammes, N.; Peer, D. Monoclonal antibody-based molecular imaging strategies and theranostic opportunities. *Theranostics* **2020**, *10*, 938−955.

(8) Yang, C.; Tian, R.; Liu, T.; Liu, G. MRI reporter genes for noninvasive molecular imaging. *Molecules* **2016**, *21*, No. 580.

(9) Pierre, V. C.; Harris, S. M.; Pailloux, S. L. Comparing strategies in the design of responsive contrast agents for magnetic resonance imaging: a case study with copper and zinc. *Acc. Chem. Res.* **2018**, *51*, 342−351.

(10) Ta, H. T.; Li, Z.; Wu, Y.; Cowin, G.; Zhang, S.; Yago, A.; Whittaker, A. K.; Xu, Z. P. Effects of magnetic field strength and particle aggregation on relaxivity of ultra-small dual contrast iron oxide nanoparticles. *Mater. Res. Express* **2017**, *4*, No. 116105.

(11) Kircher, M. F.; De La Zerda, A.; Jokerst, J. V.; Zavaleta, C. L.; Kempen, P. J.; Mittra, E.; Pitter, K.; Huang, R.; Campos, C.; Habte, F.; et al. A brain tumor molecular imaging strategy using a new triple-modality MRI-photoacoustic-Raman nanoparticle. *Nat. Med.* **2012**, *18*, 829.

(12) Tan, A. P. MRI Protocol for Craniosynostosis: Replacing Ionizing Radiation−Based CT. *Am. J. Roentgenol.* **2019**, *213*, 1374−1380.

(13) Ciesienski, K. L.; Caravan, P. Molecular MRI of Thrombosis. *Curr. Cardiovasc. Imaging Rep.* **2011**, *4*, 77−84.

(14) Cristel, G.; Brembilla, G.; Esposito, A.; Brunetti, L.; Briganti, A.; Stabile, A.; Montorsi, F.; Del Maschio, A.; De Cobelli, F. *Role of semiquantitative analysis of dynamic contrast-enhanced MRI and late gadolinium enhancement (LGE) for prostate cancer detection: may they support PI-RADS v. 2 classification?*; European Congress of Radiology, 2017.

(15) Shen, Z.; Wu, A.; Chen, X. Iron oxide nanoparticle based contrast agents for magnetic resonance imaging. *Mol. Pharmaceutics* **2017**, *14*, 1352−1364.

(16) Gaston, E.; Fraser, J. F.; Xu, Z. P.; Ta, H. T. Nano-and micro-materials in the treatment of internal bleeding and uncontrolled hemorrhage. *Nanomedicine* **2018**, *14*, 507−519.

(17) Yusof, N. N. M.; McCann, A.; Little, P. J.; Ta, H. T. Non-invasive imaging techniques for the differentiation of acute and chronic thrombosis. *Thromb. Res.* **2019**, *177*, 161−171.

(18) Liu, Y.; Wu, Y.; Zhang, R.; Lam, J.; Ng, J. C.; Xu, Z. P.; Li, L.; Ta, H. T. Investigating the use of layered double hydroxide nanoparticles as carriers of metal oxides for theranostics of ROS-related diseases. *ACS Appl. Bio Mater.* **2019**, *2*, 5930−5940.
(19) Zia, A.; Wu, Y.; Nguyen, T.; Wang, X.; Peter, K.; Ta, H. T. The choice of targets and ligands for site-specific delivery of nanomedicine to atherosclerosis. *Cardiovasc. Res.* **2020**, *116*, 2055−2068.
(20) Ta, H. T.; Li, Z.; Hagemeyer, C.; Wu, Y.; Lim, H. J.; Wang, W.; Wei, J.; Cowin, G.; Whittaker, A.; Peter, K. Novel bionanotechnological solutions based on metal oxide and metal to preserve and assess organs for transplantation. *Cryobiology* **2018**, *81*, 233.
(21) Ta, H.; Prabhu, S.; Leitner, E.; Putnam, K.; Jia, F.; Bassler, N.; Peter, K.; Hagemeyer, C. A novel biotechnological approach for targeted regenerative cell therapy and molecular imaging of atherothrombosis. *Heart, Lung Circ.* **2010**, *19*, S10.
(22) Arndt, N.; Tran, H. D.; Zhang, R.; Xu, Z. P.; Ta, H. T. Different approaches to develop nanosensors for diagnosis of diseases. *Adv. Sci.* **2020**, *7*, No. 2001476.
(23) Vazquez-Prada, K. X.; Lam, J.; Kamato, D.; Xu, Z. P.; Little, P. J.; Ta, H. T. Targeted Molecular Imaging of Cardiovascular Diseases by Iron Oxide Nanoparticles. *Arterioscler., Thromb., Vasc. Biol.* **2021**, *41*, 601−613.
(24) Wu, Y.; Zhang, R.; Tran, H. D.; Kurniawan, N. D.; Moonshi, S. S.; Whittaker, A. K.; Ta, H. T. Chitosan Nanococktails Containing Both Ceria and Superparamagnetic Iron Oxide Nanoparticles for Reactive Oxygen Species-Related Theranostics. *ACS Appl. Nano Mater.* **2021**, *4*, 3604−3618.
(25) Wu, Y.; Vazquez-Prada, K. X.; Liu, Y.; Whittaker, A. K.; Zhang, R.; Ta, H. T. Recent Advances in the Development of Theranostic Nanoparticles for Cardiovascular Diseases. *Nanotheranostics* **2021**, *5*, 499.
(26) Wu, Y.; Ta, H. T. Different approaches to synthesise cerium oxide nanoparticles and their corresponding physical characteristics, ROS scavenging and anti-inflammatory capabilities. *J. Mater. Chem. B* **2021**, DOI: 10.1039/D1TB01091C.
(27) Ta, H. T.; Arndt, N.; Wu, Y.; Lim, H. J.; Landeen, S.; Zhang, R.; Kamato, D.; Little, P. J.; Whittaker, A. K.; Xu, Z. P. Activatable magnetic resonance nanosensor as a potential imaging agent for detecting and discriminating thrombosis. *Nanoscale* **2018**, *10*, 15103−15115.
(28) Zhang, Y.; Koradia, A.; Kamato, D.; Popat, A.; Little, P. J.; Ta, H. T. Treatment of atherosclerotic plaque: perspectives on theranostics. *J. Pharm. Pharmacol.* **2019**, *71*, 1029−1043.
(29) Wu, Y.; Yang, Y.; Zhao, W.; Xu, Z. P.; Little, P. J.; Whittaker, A. K.; Zhang, R.; Ta, H. T. Novel iron oxide−cerium oxide core−shell nanoparticles as a potential theranostic material for ROS related inflammatory diseases. *J. Mater. Chem. B* **2018**, *6*, 4937−4951.
(30) Ta, H. T.; Prabhu, S.; Leitner, E.; Jia, F.; von Elverfeldt, D.; Jackson, K. E.; Heidt, T.; Nair, A. K. N.; Pearce, H.; Von Zur Muhlen, C.; et al. Enzymatic single-chain antibody tagging: a universal approach to targeted molecular imaging and cell homing in cardiovascular disease. *Circ. Res.* **2011**, *109*, 365−373.
(31) Zhang, X.-F.; Liu, Z.-G.; Shen, W.; Gurunathan, S. Silver nanoparticles: synthesis, characterization, properties, applications, and therapeutic approaches. *Int. J. Mol. Sci.* **2016**, *17*, No. 1534.
(32) Guo, D.; Zhu, L.; Huang, Z.; Zhou, H.; Ge, Y.; Ma, W.; Wu, J.; Zhang, X.; Zhou, X.; Zhang, Y.; et al. Anti-leukemia activity of PVP-coated silver nanoparticles via generation of reactive oxygen species and release of silver ions. *Biomaterials* **2013**, *34*, 7884−7894.
(33) Liu, F.; Mahmood, M.; Xu, Y.; Watanabe, F.; Biris, A. S.; Hansen, D. K.; Inselman, A.; Casciano, D.; Patterson, T. A.; Paule, M. G.; et al. Effects of silver nanoparticles on human and rat embryonic neural stem cells. *Front. Neurosci.* **2015**, *9*, No. 115.
(34) Gonzalez-Carter, D. A.; Leo, B. F.; Ruenraroengsak, P.; Chen, S.; Goode, A. E.; Theodorou, I. G.; Chung, K. F.; Carzaniga, R.; Shaffer, M. S.; Dexter, D. T.; et al. Silver nanoparticles reduce brain inflammation and related neurotoxicity through induction of H 2 S-synthesizing enzymes. *Sci. Rep.* **2017**, *7*, No. 42871.
(35) Ammari, H.; Deng, Y.; Millien, P. Surface plasmon resonance of nanoparticles and applications in imaging. *Arch. Ration. Mech. Anal.* **2016**, *220*, 109−153.
(36) Xu, G.; Chen, Y.; Tazawa, M.; Jin, P. Surface plasmon resonance of silver nanoparticles on vanadium dioxide. *J. Phys. Chem. B* **2006**, *110*, 2051−2056.
(37) Jaque, D.; Maestro, L. M.; Del Rosal, B.; Haro-Gonzalez, P.; Benayas, A.; Plaza, J.; Rodriguez, E. M.; Sole, J. G. Nanoparticles for photothermal therapies. *Nanoscale* **2014**, *6*, 9494−9530.
(38) Jain, P. K.; Huang, X.; El-Sayed, I. H.; El-Sayed, M. A. Noble metals on the nanoscale: optical and photothermal properties and some applications in imaging, sensing, biology, and medicine. *Acc. Chem. Res.* **2008**, *41*, 1578−1586.
(39) Takahashi, I.; Emi, Y.; Hasuda, S.; Kakeji, Y.; Maehara, Y.; Sugimachi, K. Clinical application of hyperthermia combined with anticancer drugs for the treatment of solid tumors. *Surgery* **2002**, *131*, S78−S84.
(40) Zhang, B.; Wang, H.; Shen, S.; She, X.; Shi, W.; Chen, J.; Zhang, Q.; Hu, Y.; Pang, Z.; Jiang, X. Fibrin-targeting peptide CREKA-conjugated multi-walled carbon nanotubes for self-amplified photothermal therapy of tumor. *Biomaterials* **2016**, *79*, 46−55.
(41) Ma, L. L.; Feldman, M. D.; Tam, J. M.; Paranjape, A. S.; Cheruku, K. K.; Larson, T. A.; Tam, J. O.; Ingram, D. R.; Paramita, V.; Villard, J. W.; et al. Small multifunctional nanoclusters (nanoroses) for targeted cellular imaging and therapy. *ACS Nano* **2009**, *3*, 2686−2696.
(42) Kosuge, H.; Sherlock, S. P.; Kitagawa, T.; Dash, R.; Robinson, J. T.; Dai, H.; McConnell, M. V. Near infrared imaging and photothermal ablation of vascular inflammation using single-walled carbon nanotubes. *J. Am. Heart Assoc.* **2012**, *1*, No. e002568.
(43) Shao, J.; Griffin, R. J.; Galanzha, E. I.; Kim, J.-W.; Koonce, N.; Webber, J.; Mustafa, T.; Biris, A. S.; Nedosekin, D. A.; Zharov, V. P. Photothermal nanodrugs: potential of TNF-gold nanospheres for cancer theranostics. *Sci. Rep.* **2013**, *3*, No. 1293.
(44) Deng, H.; Dai, F.; Ma, G.; Zhang, X. Theranostic gold nanomicelles made from biocompatible comb-like polymers for thermochemotherapy and multifunctional imaging with rapid clearance. *Adv. Mater.* **2015**, *27*, 3645−3653.
(45) Liu, Y.; Xu, M.; Chen, Q.; Guan, G.; Hu, W.; Zhao, X.; Qiao, M.; Hu, H.; Liang, Y.; Zhu, H.; Chen, D. Gold nanorods/mesoporous silica-based nanocomposite as theranostic agents for targeting near-infrared imaging and photothermal therapy induced with laser. *Int. J. Nanomed.* **2015**, *10*, No. 4747.
(46) Fu, D.; Liu, J.; Ren, Q.; Ding, J.; Ding, H.; Chen, X.; Ge, X. Magnetic Iron Sulfide Nanoparticles as Thrombolytic Agents for Magnetocaloric Therapy and Photothermal Therapy of Thrombosis. *Front. Mater.* **2019**, No. 316.
(47) Singh, N.; Varma, A.; Verma, A.; Maurya, B. N.; Dash, D. Relief from vascular occlusion using photothermal ablation of thrombus with a multimodal perspective. *Nano Res.* **2016**, *9*, 2327−2337.
(48) Shi, J.; Wang, L.; Zhang, J.; Ma, R.; Gao, J.; Liu, Y.; Zhang, C.; Zhang, Z. A tumor-targeting near-infrared laser-triggered drug delivery system based on GO@ Ag nanoparticles for chemo-photothermal therapy and X-ray imaging. *Biomaterials* **2014**, *35*, 5847−5861.
(49) Sharma, R.; Agrawal, U.; Mody, N.; Dubey, S.; Vyas, S. P. Engineered Nanoparticles as a Precise Delivery System in Cancer Therapeutics. In *Engineering of Nanobiomaterials*; Elsevier, 2016; pp 397−427.
(50) Liu, Y.; Wu, Y.; Zhang, R.; Lam, J.; Ng, J. C.; Xu, Z.-P.; Li, L.; Ta, H. T. Investigating the Use of Layered Double Hydroxide Nanoparticles as Carriers of Metal Oxides for Theranostics of ROS-Related Diseases. *ACS Appl. Bio Mater.* **2019**, *2*, 5930−5940.
(51) Hagerty, P.; Lee, A.; Calve, S.; Lee, C. A.; Vidal, M.; Baar, K. The effect of growth factors on both collagen synthesis and tensile strength of engineered human ligaments. *Biomaterials* **2012**, *33*, 6355−6361.

https://doi.org/10.1021/acsanm.1c01571
ACS Appl. Nano Mater. XXXX, XXX, XXX−XXX

(52) Lou, X. W.; Yuan, C.; Archer, L. A. An unusual example of hyperbranched metal nanocrystals and their shape evolution. *Chem. Mater.* **2006**, *18*, 3921−3923.
(53) Brown, K. R.; Natan, M. J. Hydroxylamine seeding of colloidal Au nanoparticles in solution and on surfaces. *Langmuir* **1998**, *14*, 726−728.
(54) Dasri, T.; Chingsungnoen, A. Surface plasmon resonance enhanced light absorption and wavelength tuneable in gold-coated iron oxide spherical nanoparticle. *J. Magn. Magn. Mater.* **2018**, *456*, 368−371.
(55) Pensa, E.; Cortes, E.; Corthey, G.; Carro, P.; Vericat, C.; Fonticelli, M. H.; Benitez, G.; Rubert, A. A.; Salvarezza, R. C. The chemistry of the sulfur−gold interface: in search of a unified model. *Acc. Chem. Res.* **2012**, *45*, 1183−1192.
(56) Ansar, S. M.; Fellows, B.; Mispireta, P.; Mefford, O. T.; Kitchens, C. L. pH triggered recovery and reuse of thiolated poly (acrylic acid) functionalized gold nanoparticles with applications in colloidal catalysis. *Langmuir* **2017**, *33*, 7642−7648.
(57) Raj, D. R.; Prasanth, S.; Vineeshkumar, T.; Sudarsanakumar, C. Surface plasmon resonance based fiber optic dopamine sensor using green synthesized silver nanoparticles. *Sens. Actuators, B* **2016**, *224*, 600−606.
(58) Baffou, G.; Quidant, R.; Girard, C. Heat generation in plasmonic nanostructures: Influence of morphology. *Appl. Phys. Lett.* **2009**, *94*, No. 153109.
(59) Amendola, V.; Pilot, R.; Frasconi, M.; Maragò, O. M.; Iatì, M. A. Surface plasmon resonance in gold nanoparticles: a review. *J. Phys.: Condens. Matter* **2017**, *29*, No. 203002.
(60) Baffou, G.; Quidant, R. Thermo-plasmonics: using metallic nanostructures as nano-sources of heat. *Laser Photonics Rev.* **2013**, *7*, 171−187.
(61) Mackey, M. A.; Ali, M. R.; Austin, L. A.; Near, R. D.; El-Sayed, M. A. The most effective gold nanorod size for plasmonic photothermal therapy: theory and in vitro experiments. *J. Phys. Chem. B* **2014**, *118*, 1319−1326.
(62) Zhang, Z.; Mascheri, N.; Dharmakumar, R.; Li, D. Cellular magnetic resonance imaging: potential for use in assessing aspects of cardiovascular disease. *Cytotherapy* **2008**, *10*, 575−586.
(63) Forman, H. J.; Torres, M. Redox signaling in macrophages. *Mol. Aspects Med.* **2001**, *22*, 189−216.
(64) Zhang, L.; Wu, L.; Si, Y.; Shu, K. Size-dependent cytotoxicity of silver nanoparticles to Azotobacter vinelandii: Growth inhibition, cell injury, oxidative stress and internalization. *PLoS One* **2018**, *13*, No. e0209020.
(65) Walski, T.; Dyrda, A.; Dzik, M.; Chludzińska, L.; Tomków, T.; Mehl, J.; Detyna, J.; Gałecka, K.; Witkiewicz, W.; Komorowska, M. Near infrared light induces post-translational modifications of human red blood cell proteins. *Photochem. Photobiol. Sci.* **2015**, *14*, 2035−2045.

■ NOTE ADDED AFTER ASAP PUBLICATION

This paper was published ASAP on September 2, 2021, with errors in Fig. 1 and the Supporting Information. These were corrected in the version published ASAP on September 3, 2021.

https://doi.org/10.1021/acsanm.1c01571
ACS Appl. Nano Mater. XXXX, XXX, XXX−XXX

Supporting information

Silver/Iron Oxide Nano-popcorns for Imaging and Therapy

Ateeque ur Rehman[1,2], Yuao Wu[1,4,#], Huong D.N. Tran[1,4,#], Karla Vazquez-Prada[1,4], Yajun Liu[4], Hossein Adelnia[1,4], Nyoman D. Kurniawan[5], Muhammad Naeem Anjum[2], Shehzahdi S. Moonshi[1], Hang T. Ta[1,3,4,*]

[1]Queensland Micro- and Nanotechnology Centre, Griffith University, Brisbane, 4111, Australia

[2]Department of Physics, the Islamia University of Bahawalpur, Punjab, 63100, Pakistan

[3]School of Environment and Science, Griffith University, Brisbane, 4111, Australia

[4]Australian Institute for Bioengineering and Nanotechnology, University of Queensland, Brisbane, 4072, Australia

[5]Centre for Advanced Imaging, University of Queensland, Brisbane, 4072, Australia

[#]Equal contribution

*Correspondence to Hang T. Ta (h.ta@griffith.edu.au)

Materials and Methods

All reagents and solvents were obtained from standard commercial sources and were used as received. All chemicals were purchased from Sigma-Aldrich. Phosphate-buffered saline (PBS), Dulbecco's modified eagle medium (DMEM), RPMI 1640 medium, fetal bovine serum (FBS), penicillin-streptomycin solution, L-glutamine, non-essential amino acids solution (100X), PrestoBlue® cell viability reagent and TrypLE™ Express were purchased from ThermoFisher Scientific.

Synthesis of iron oxide nanoparticles (IONPs)

IONPs were synthesised using a high-temperature co-precipitation method. Briefly, $FeCl_3 \cdot 6H_2O$ (0.2 M) and $(NH_4)_2Fe(SO_4)_2 \cdot 6H_2O$ (0.1 M) were dissolved in 50 mL milliQ water with constant stirring at 80°C under nitrogen flow for 30 min. 1M NaOH solution was added dropwise to co-precipitate the iron until pH=12. After 15 min, IONPs were separated by centrifugation and the precipitate was washed with milliQ water and then with 1M HCl, followed by incubation with 0.1 M trisodium citrate (TSC) at 80°C for 6 hr under constant stirring. The citrate-coated IONPs were sonicated, centrifuged at 8000 rpm, and dialysed against milliQ water.

Synthesis of silver/iron oxide hybrid nano-popcorn (Ag@IO)

To obtain the silver coating on the surface of the IONPs, $AgNO_3$ (200 µL, 6.348mM) was added into 8.8 mL miliQ water followed by the addition of the IONPs (178 µL, stock [Fe]=0.808 mg/mL) synthesised before. The elemental silver was seeded and reduced on the surface of IONPs by of hydroxylamine (20 µL, 50%), and TSC (150 µL, 1.14%) was added to stabilise the nanoparticles. The dense silver-coated IONPs were separated from the less dense

uncoated particles by centrifugation at 4000 x *g* for 6 min, redispersed in milliQ water and then dialysed against water overnight to remove any un-reacted reagents.

Thiolation of PAA and coating of Ag@IO with PAA-SH

Synthesis of PAA-SH was carried out by dissolving PAA (0.1 g, 1800 g/mol) in DMSO (5 mL). N-Hydroxysuccinimide (NHS) and 1-Ethyl-3-(3-dimethylaminopropyl)carbodiimide (EDC) were added in a 1:1 molar ratio (EDC to NHS), and in a 5:1 molar ratio (COOH to EDC). After stirring for 30 min, cysteamine was added to the solution in a 5:1 ratio (COOH to SH) and left stirring for 4 hr. PAA-SH was precipitated by addition of toluene in a 1:5 volume ratio (PAA-SH in toluene) followed by centrifugation. PAA-SH (18 mg) was dissolved in water (2 mL) and pH was adjusted to 7 with NaOH 1M. Subsequently, Ag@IO (1 mg) was added to the above solution under continuous stirring overnight. Ag@IO-PAA was washed twice with milliQ water.

Conjugation of platelet-binding peptide to Ag@IO-PAA

EDC (592.6 nmoles) was added to MES buffer (2 mL, pH 4.9) containing 1.6 mg of Ag@IO-PAA and incubated at room temperature. After 15 min, the nanoparticles were collected by centrifugation at 8000 rpm for 15 min. The particles were then resuspended in PBS (pH 7.2) and 3.5 µmoles RGD peptide was added. The mixture was incubated overnight at room temperature, followed by washing the Ag@IO-PAA-RGD nanoparticles with water twice.

Characterisation of the nano-popcorns

Hydrodynamic size, size distribution and zeta potential (ZP) of the nanoparticles were measured by dynamic light scattering (DLS) using a Zetasizer Nano ZS (Malvern). Transmission electron microscopy (TEM) images were taken on a JEOL-JEM-1010, operating at an accelerating voltage of 100 kV. Energy-Dispersive X-ray Spectroscopy (EDS) was carried

out with HT7700 TEM (Hitachi) and analysed on an XFlash6TI60 (Bruker). The concentrations of iron and silver were determined by inductively coupled plasma-optical emission spectroscopy (ICP-OES) (Optima 8300DV ICP-OES from Perkin Elmer). To analyse the surface coating of the nanoparticles, Fourier Transform Infrared Spectroscopy (FTIR) spectra were obtained by a Nicolet 5700 FTIR.

The transverse relaxivity of the nanoparticles was measured with a Bruker 9.4T MRI scanner. For MRI, phantom vessels containing 100 µl of different concentrations of the nanoparticles were prepared in triplicates. The phantom tubes were embedded in Eppendorf tubes containing 1% agarose. T_2 weighted images were acquired with the following parameters: field of view = 58mm x 58mm, image size= 256x256, slice thickness= 1mm, TR=2000ms, TE=75ms.

Cell culture

Chinese hamster ovary (CHO), macrophage J774A.1, and MDA-MB-231 lines were attained from the American Type Culture Collection (ATCC). CHO cells were cultured in 75 cm^2 flask containing DMEM supplemented with FBS (10%), penicillin (100 U/mL), streptomycin (100 µg /mL) and non-essential amino acids (1%). For the macrophages, non-treated 100×20mm cell culture dish was used with RPMI 1640 with FBS (10%), penicillin (100 U/mL) and L-glutamine (1%). MDA-MB-231 cells were maintained in 75 cm^2 flask containing DMEM supplemented with FBS (10%), penicillin (100 U/mL) and streptomycin (100 µg /mL). All these three cell lines were cultured at 37 ℃ with 5% CO_2.

Cytotoxicity study

At confluence, the cells were detached, and seeded into 96-well plate at a density of 10,000 cells/well. CHO and MDA-MB-231 cells were detached with TrypLE™ express for 5 min at 37 °C, while macrophages were detached with cold PBS. After 24 hr incubation, the cells were treated with different concentrations of nanoparticles (0, 0.01, 0.05, 0.1, and 0.2 mg/ml). After

24 hr nanoparticle treatment, the cell viability was determined by treating cells with PrestoBlue® cell viability reagent for 30 min. The fluorescence intensity was measured by microplate reader with excitation and emission wavelengths of 560, and 590 nm, respectively. The fluorescence of the control group (i.e., without nanoparticle treatment) was considered as 100% cell viability. MDA-MB-231 cells were also treated with ethidium homodimer-1 fluorescence dye (1μM) for 30 min to detect dead macrophages. The fluorescence image was taken by Nikon ECLIPSE Ti microscopy system with Photometrics® CoolSNAPTM HQ2 camera and Nikon Intensilight C-HGFIE fluorescence light source.

ROS scavenging

Nanoparticles (0, 0.005, 0.01, 0.05, 0.1, and 0.2 mg/ml) were treated with H_2O_2 (0.1 mM) in 96-well plate for 1 hr at 37 ºC with shaking (200 rpm). 0.01 unit of horseradish peroxidase (HRP) was added into each reaction followed by 10 min incubation at room temperature. 8.7mM of 2,20-azino-bis(3-ethylbenzothiazoline-6-sulphonic acid (ABTS) was then added into the reaction and the absorbance of samples at 405 nm was measured by microplate reader. The absorbance of 0 μg/ml sample was determined as 0 % ROS scavenging.

Cellular ROS was evaluated with 2',7' –dichlorofluorescein diacetate (DCFDA) as previously described [45]. Briefly, macrophages were seeded in 96-well tissue-treated plates at a density of 10,000 cells/well. After 24 h incubation, macrophages were treated with the nanoparticles at the concentration ranging from 0 to 0.05 mg/mL. After four-hour treatment with NPs to allow NP uptake by macrophages, the NP solution was removed, followed by adding 100 μL of DCFDA (25 μM final concentration) diluted in PBS, incubated for 45 min and washed with PBS once. The intracellular levels of ROS were stimulated by 0.5 mM H_2O_2 dissolved in PBS and determined by recording the fluorescence intensity at 15 min after adding H_2O_2. Fluorescence intensity was measured (Excitation/Emission = 485/535 nm) using an EnSpire

Alpha Multimode Plate Reader (PerkinElmer). The background fluorescence value containing cell-only control wells was subtracted from the fluorescence value of each experimental well. ROS levels were calculated using the following equation:

$$\text{ROS level (fold change)} = \frac{F_{stimulation}}{F_{control}}$$

Where $F_{stimulation}$ was the fluorescence intensity of the cells stimulated by H_2O_2 and $F_{control}$ was the fluorescence intensity of the cells treated with DCFDA only without any additional stimulation. The fluorescence images were taken by Nikon ECLIPSE T*i* microscopy system with Photometrics® CoolSNAP™ HQ^2 camera and Nikon INTENSILIGHT C-HGFIE fluorescent light source.

In vitro cell and thrombus MRI

Cancer cells (MDA-MB-231), and macrophages (J774A.1) were seeded in 6-well plates at a density of 2 x 10^5, and 3 × 10^5 cells/well, respectively. After 24 h, the cells were treated with Ag@IO-PAA (0.1 mg/mL). After an additional 12 hr incubation, the nanoparticle-containing medium was discarded and the cells were washed with PBS once. The cells were then detached by TrypLE Express and centrifuged at 200 x *g* for 5 min. TrypLE Express was removed after washing the cells with PBS at 200 x *g* for 5 min. The cells were subsequently resuspended in 20 μL of warm 1% low-gelling temperature agarose and quickly transferred into the prepared phantom vessel as described previously. The prepared phantom vessel was then embedded in a 1.5 mL Eppendorf tube containing 1% agarose gel. MRI was performed on a 9.4 T MRI scanner (Bruker). T_2-weighted images were captured under the following parameter settings: TR = 2000 ms, TE = 25 ms, bandwidth 100,000 Hz.

In vitro thrombus was prepared by adding a mixture containing 100 μL of fresh frozen plasma (obtained from Australian Red Cross Blood Service), $CaCl_2$ (2.5 μL, 1M) into a 1.5 mL

Eppendorf tube and incubated at 37°C for 10 min. Ag@IO-PAA-RGD nanoparticle dispersion (50 μL, 1.6 mg/mL) was added on top of the thrombus and the tube was incubated with gentle rotation for 1 hr at 37°C. The thrombus was then washed 3 times with PBS. Agarose gel (100 μL, 1%) was added on top of the thrombus and allowed to solidify at room temperature. MRI was performed on a 9.4 T MRI scanner (Bruker). T_2-weighted images were captured under the following parameter settings: TR = 2348 ms, TE = 25 ms, bandwidth 50,000 Hz.

Photothermal thrombolysis

In vitro human thrombi were prepared from human whole blood provided by the Australian Red Cross. Briefly, whole blood (50 μl) was mixed with $CaCl_2$ (1.25 μL, 1 M), Actin FSL (4 μL) (Siemens) and PBS (60 μL) in a glass vial by careful pipetting to minimise bubble formation. Any air bubble that formed was popped with a needle. The mixture was incubated for 15 min at room temperature. 100 μL of nanoparticle dispersion at different concentrations (0, 0.1, 0.2, 0.4, 0.6, 0.8 mg/mL in PBS) was added and incubated at room temperature for 1 hr. The weight of glass vials was measured before and after the experiment and the initial and final temperatures were also recorded with a thermal camera (FLIR, US). The thrombi were irradiated with an 808 nm infrared laser (light intensity= 1.59 W/cm^2, beam diameter= 2 cm) for 2 min in a custom-built stabilised infrared fibre laser system. After the laser exposure, the liquid remaining of the lysis was discarded and the clot mass loss was calculated for each thrombus. The mass loss percentage was normalised against that of the thrombus with no treatment or PBS.

Photothermal cancer cell treatment

Human breast cancer cells (MDA-MB-231) were cultured in 24-well plate at 50,000 cells/well for 1 day. Cells were then incubated with different concentrations of the nanoparticles (0, 0.01, 0.05, 0.1, 0.2 mg/mL). After 1 day, the cells were washed with PBS and irradiated with an 808

nm infrared laser (light intensity= 1.59W/cm^2, beam diameter= 2 cm) for 2 min. Cell viability was evaluated using PrestoBlue® cell viability reagent as described above.

Hemolysis assay

The percent of hemolysis was measured at 4 and 24 hrs hours. Briefly, red blood cells were obtained by centrifugation of whole blood at 1000 rpm for 15 min. The pellet was washed twice and resuspended (1:50) with PBS (pH=7.4). Immediately, 180 µL of the red blood cells solution was incubated at 37°C with increasing concentrations of the nano-popcorns (20 µL) and mild shaking. The incubated red blood cells were then centrifuged (1000 rpm for 15 min) and the supernatant was collected. Absorbance was measured at 545 nm using a microplate reader (FLUOstar Omega microplate reader, BMG LABTECH). Plasma hemoglobin was estimated to calculate the percentage of hemolysis by the following equation:

$$\text{Hemolysis (\%)} = \frac{\text{OD sample} - \text{OD negative control}}{\text{OD positive control} - \text{OD negative control}}\ x\ 100$$

Histology and in vivo biodistribution

Animal study was conducted at the University of Queensland (Brisbane, Australia). Care and use of laboratory animal followed the national guidelines and were approved by the institutional animal care and ethics committees of the University of Queensland. 5-month old C57BL/6 wild-type mice (Animal Resources Centre, ARC, Western Australia) were injected with the nanoparticles at a dose of 3.2 mg/kg mouse. The mice were sacrificed at 1, 3, 7 days post injection and organs (heart, lung, kidney, liver, spleen) were collected for analysis. Control mice are those injected with just PBS. The collected organs were washed in PBS and fixed with paraformaldehyde (4% w/v).

For histology analysis, samples were cut into 10 µm thick cross-sections and stained with haemotoxylin and eosin (H&E). Histology images were taken using an inverted microscope

(IX51, Olympus) with digital colour camera (Olympus) and QCapture Pro6.0 software (QImaging).

For biodistribution analysis, the organs were dissolved in aqua regia for 3 days at room temperature. The lysis solutions were centrifuged at 16,000 x *g* for 5 min to remove all debris and then diluted 1:10 for inductively coupled plasma mass spectrometry (ICP-MS) analysis. ICP-MS was used to detect the content of Ag in the organs.

Statistical Analyses

Data are presented as mean ± SD from at least three independent experiments and analysed with two-way ANOVA or one-way ANOVA. The level of statistical significance was defined as p-value < 0.05. The graphs were plotted using GraphPad Prism 7 software (GraphPad Prism Inc. CA, USA).

Additional Results

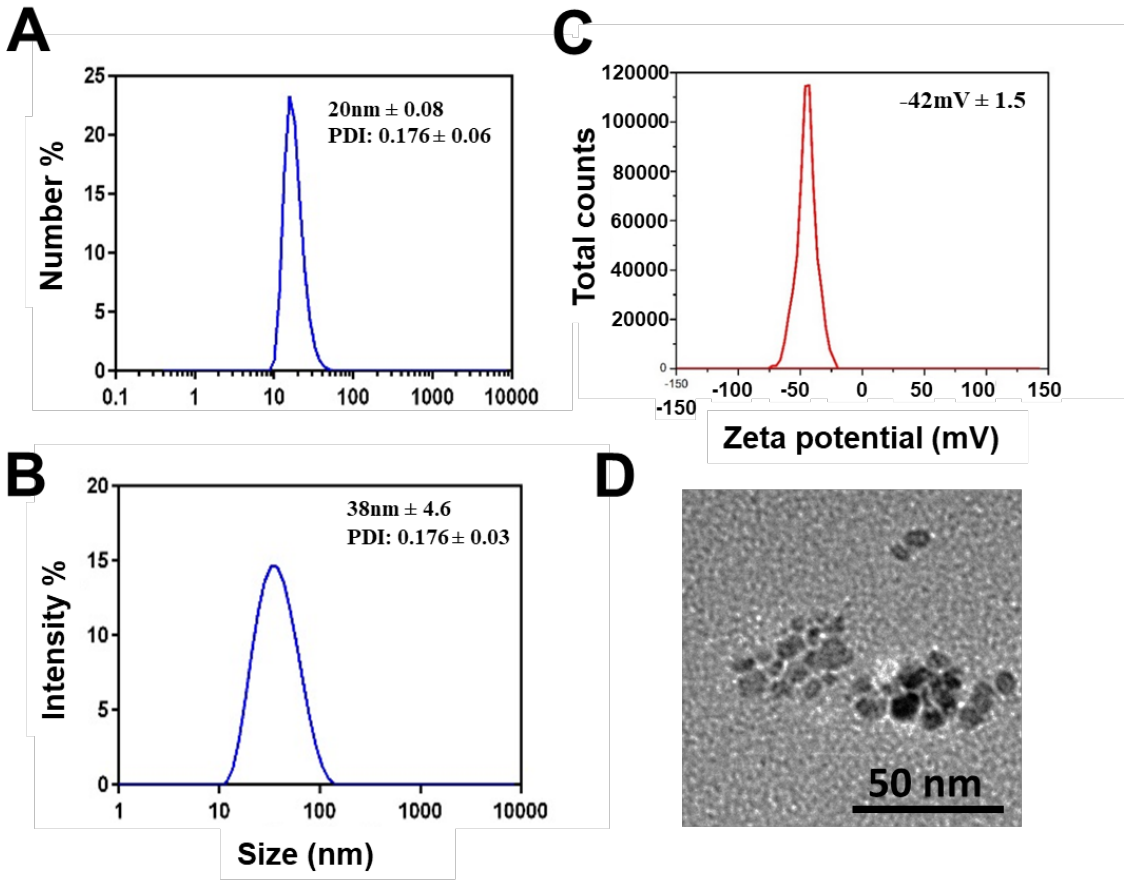

Figure S1: Characterisation of iron oxide nanoparticles (IONPs). (A), **(B)** Size distribution obtained from DLS. **(C)** ZP of the nano-popcorns obtained from DLS. **(D)** TEM image of IONPs (scale bar = 100 nm).

Table S1: DLS data of the coated and bare nanoparticles

Nanoparticles	Number mean (nm)	Intensity mean (nm)	PDI	Zeta potential (mV)
IONP	20±0.08	38±4.6	0.176±0.03	-42±1.5
Ag@IO	89±0.19	105±0.16	0.056±0.004	-24±2.1
Ag@IO-PAA	113±1.2	120±0.17	0.086 ± 0.05	-38 ± 1.8

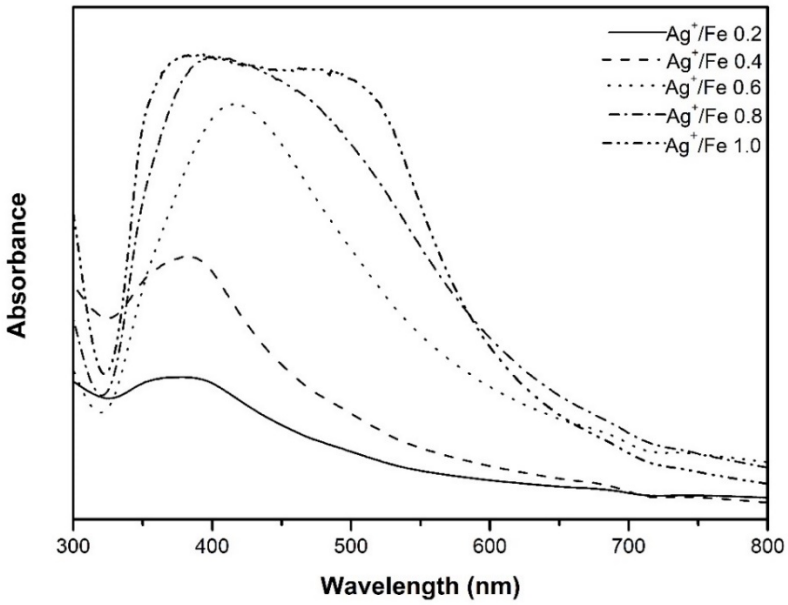

Figure S2: Optimization of the concentration of silver using 2 µL HDX, 150 µL TSC at the different Ag^+/Fe ratio (0.2, 0.4, 0.6, 0.8, 1.0).

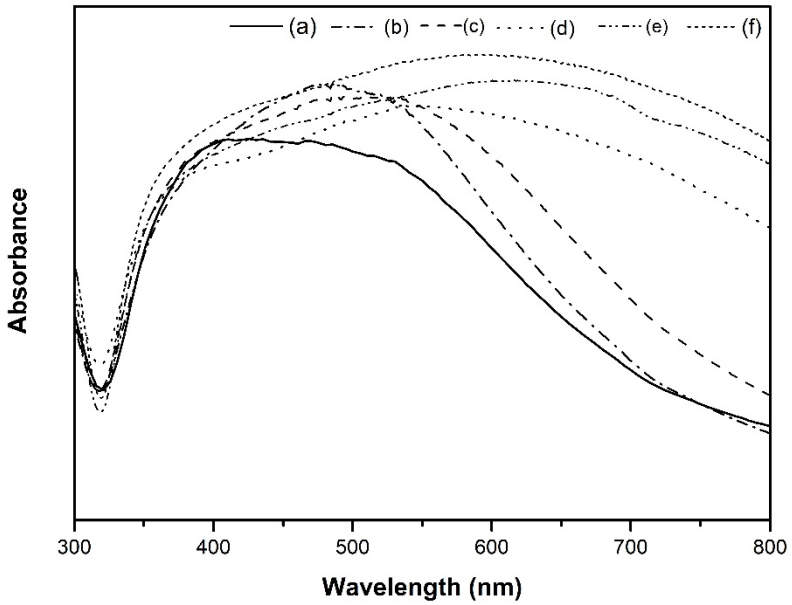

Figure S3: Effects of varying amount of hydroxylamine to reduce silver ions on the surface of IONPs: 2 (a); 4 (b); 6 (c); 8 (d); 10 (e); and 20 µL (f). Ag^+/Fe ratio was kept at 1.

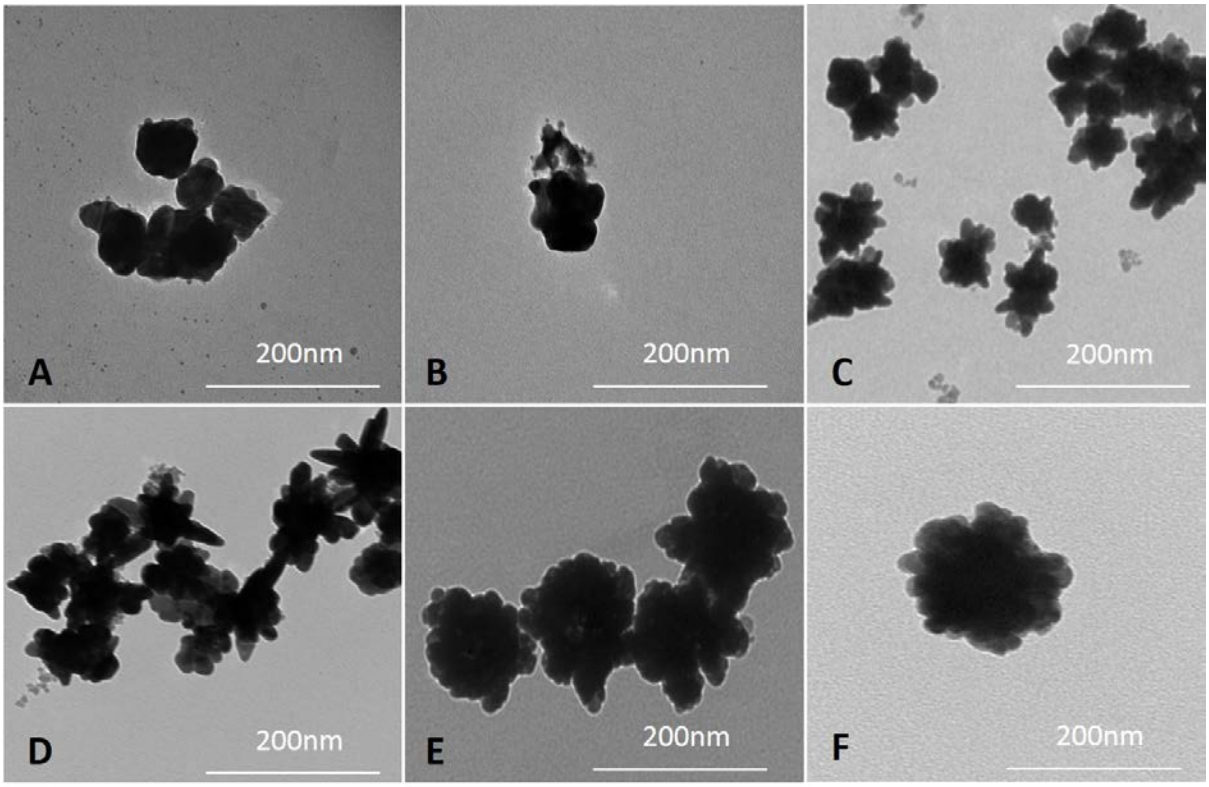

Figure S4: TEM micrographs for the morphological observation of nucleation and growth of silver nanoparticles. Improper growth of silver ions by using different amount of hydroxylamine. (A) 2 µL, (B) 4 µL, (C) 6 µL, (D) 8 µL, (E) 10 µL; Homogeneous and proper nano-popcorns by using 20 µL hydroxylamine and 150 µL TSC (F)

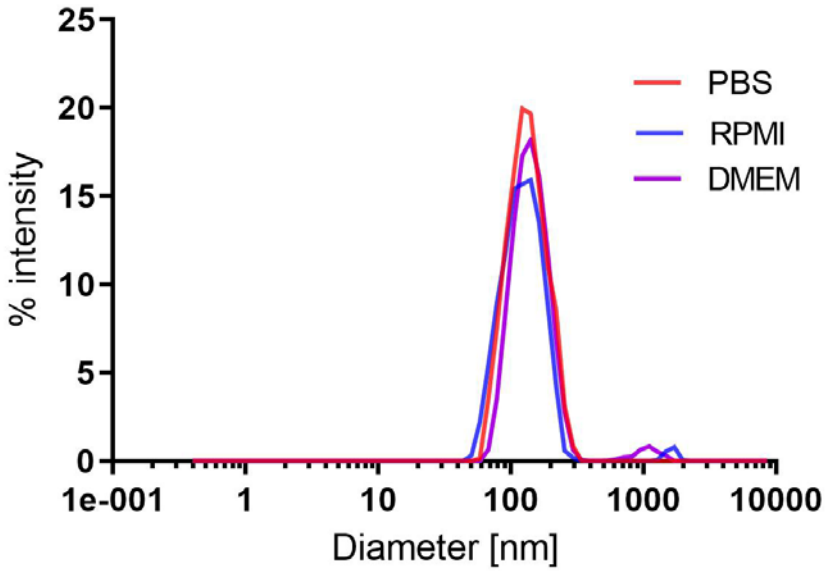

Figure S5: Dynamic light scattering analysis of the Ag@IO-PAA in different media after 2 weeks. The graph shows that these nanoparticles have relatively good stability in the three different media (PBS, RPMI, DMEM). Very small agglomeration was noted in RPMI and DMEM solution. The samples were briefly sonicated in a sonication bath before measurement.

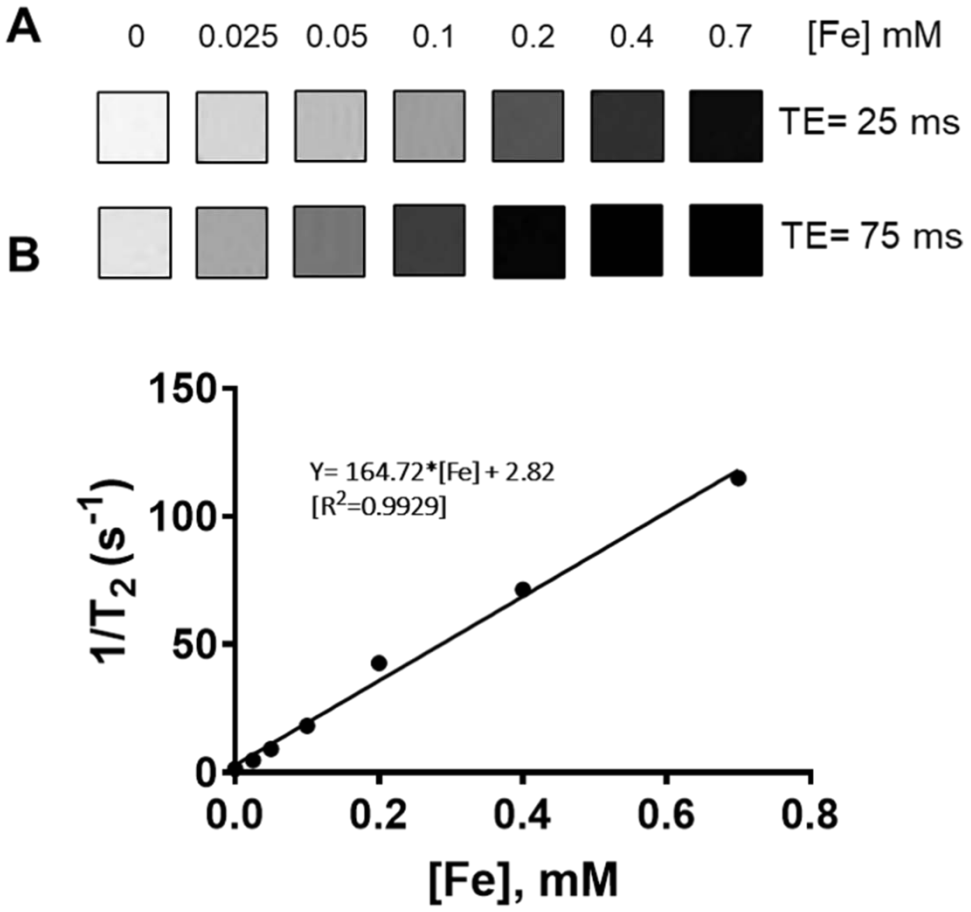

Figure S6: MRI of IONP. (A) T_2-weighted images of IONP prepared in phantoms at different concentrations, acquired using 9.4 T MRI scanner at different TE. (B) Plot of relaxation rates $1/T_2$ versus Fe concentrations of IONP.

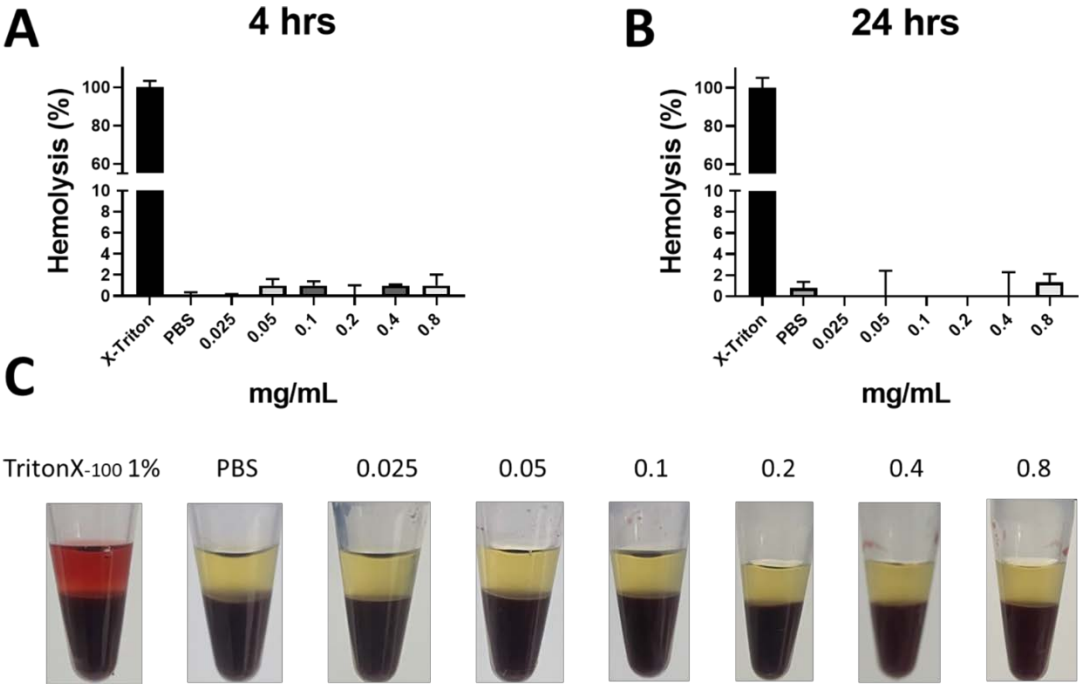

Figure S7. Hemolysis rate of the nano-popcorns at different concentrations (0.025 – 0.8 mg/mL) at (A) 4 and (B) 24 h. PBS pH 7.4 was used as negative control and TritonX-100 1% was used as positive control. (C) Visual inspection of tubes containing diluted red blood cells after exposure to nano-popcorns.